

THE SEARCH FOR EXOMOON

RADIO EMISSIONS

by

JOAQUIN P. NOYOLA

Presented to the Faculty of the Graduate School of
The University of Texas at Arlington in Partial Fulfillment
of the Requirements
for the Degree of

DOCTOR OF PHILOSOPHY

THE UNIVERSITY OF TEXAS AT ARLINGTON

December 2015

Copyright © by Joaquin P. Noyola 2015

All Rights Reserved



Dedicated to my wife Thao Noyola, my son Layton, my daughter Allison, and our future
little ones.

Acknowledgements

I would like to express my sincere gratitude to all the people who have helped throughout my career at UTA, including my advising professors Dr. Zdzislaw Musielak (Ph.D.), and Dr. Qiming Zhang (M.Sc.) for their advice and guidance. Many thanks to my committee members Dr. Andrew Brandt, Dr. Manfred Cuntz, and Dr. Alex Weiss for your interest and for your time. Also many thanks to Dr. Suman Satyal, my collaborator and friend, for all the fruitful discussions we have had throughout the years.

I would like to thank my wife, Thao Noyola, for her love, her help, and her understanding through these six years of marriage and graduate school.

October 19, 2015

Abstract

THE SEARCH FOR EXOMOON

RADIO EMISSIONS

Joaquin P. Noyola, PhD

The University of Texas at Arlington, 2015

Supervising Professor: Zdzislaw Musielak

The field of exoplanet detection has seen many new developments since the discovery of the first exoplanet. Observational surveys by the NASA Kepler Mission and several other instrument have led to the confirmation of over 1900 exoplanets, and several thousands of exoplanet potential candidates. All this progress, however, has yet to provide the first confirmed exomoon. Since all previous attempts to discover exomoons have failed, a novel method to detect them is proposed in this dissertation, which describes development of the method and its applications to select the best exomoon candidates for observational searches. The main goal of these searches is to verify the validity and effectiveness of the method, and discover the first exomoon by using the world largest and most suitable radio telescopes. The discovery of first exomoon would begin a new era of exploratory research in exoplanetary systems.

The idea that exomoons can be discovered with radio telescopes was first proposed by Musielak & Musielak (2011), and then developed by Noyola, Satyal & Musielak (2014). They suggested that the interaction between Io and the Jovian magnetosphere could also be found in exoplanet-exomoon pairs, and the resulting radio emissions could be used to directly detect these systems. The main results of the 2014 study obtained for single prograde exomoons are also described in this dissertation, which in addition extends the previous study to multiple exomoon systems, as well as

retrograde orbits. The main objective of these studies is to identify the best exomoon candidates for detection by chosen radio telescopes. One such candidate, Epsilon Eridani b, was selected and observed by the Giant Metre Radio Telescope (GMRT) in India. The preliminary results of these observations do not show any expected radio emission from the chosen systems. Thus, implementation of several important improvements to the method is discussed in details in this dissertation.

Table of Contents

Acknowledgements	iv
Abstract	v
List of Illustrations	ix
Chapter 1 Introduction.....	1
1.1 The Transit Method	2
1.2 The Radial Velocity Method.....	5
1.3 Radio Detection	6
1.4 Other Detection Techniques.....	7
1.5 Exoplanet Statistics	9
1.6 The New Frontier	10
Chapter 2 Planetary Magnetospheres	11
2.1 Magnetosphere Topology	11
2.2 Modeling Planetary Magnetic Fields.....	15
2.3 Magnetic Dipole Moment Approximation.....	19
Chapter 3 Moon Systems.....	22
3.1 Io and the Galilean Moons.....	23
3.2 Notes on Moon Formation	24
Chapter 4 Theory of Exomoon Radio Signals.....	27
4.1 Planetary Radio Emissions.....	27
4.2 Unipolar Induction Mechanism	29
4.3 Moons as Unipolar Inductors: Electromotive Moons	30
4.4 Generation and Role of Alfvén Waves	32
4.5 Signal Frequency, Bandwidth, and Periodicity	33
4.6 Intensity of the Radio Emissions	35

4.7 Parameters and Assumptions	37
4.8 Detectability Limits.....	42
4.9 Possibility of False Positives	46
Chapter 5 Multiple-Moon Detections Through Plasma Torus Sharing	48
5.1 Plasma Torus Topology.....	48
5.2 Corotation Plasma Velocity	50
5.3 Signal Power and Flux density	53
5.4 Physical Properties Derived from Multiple Detections.....	55
5.5 More Plasma Sources	56
Chapter 6 Exomoon Radio Detection	58
6.1 Previous Detection Attempts	58
6.2 Prospective Observational Facilities	58
6.2.1 LWA and LOFAR.....	59
6.2.2 GMRT	61
6.2.3 SKA	64
6.2.4 Other Facilities.....	64
Chapter 7 Prospective Research Plans	66
Chapter 8 Concluding Remarks.....	68
Appendix A Successful Observational Proposal.....	69
Appendix B Simulation Program to Calculate Exomoon Radio Power.....	80
References.....	87
Biographical Information	93

List of Illustrations

Figure 1.1. Properties and examples of transit events. Panel (c) taken from (Campante, et al., 2015). Other Image Credits: panel (e) Suman Satyal, panel (f) Billy Quarles.	4
Figure 1.2. Radial velocity diagram. The exoplanet causes the star to wobble around the center of mass, which in turn causes a Doppler shift in the star light's wavelength.	5
Figure 1.3. Gravitational microlensing by an exoplanet. © NASA, ESA, and A. Feild (STScI)	8
Figure 1.4. Direct Imaging of HR 8799bcde at 24, 38, 68, and 14.5 AU; ~39pc from Earth (~127 ly). Using Keck & Gemini. Taken from (Marois, et al., 2010).	9
Figure 1.5. Mass and period distribution of all confirmed exoplanets, color coded by their detection method.....	10
Figure 2.1. Structure of a magnetosphere with its major parts labeled. The major parts are 1) the bowshock, 2) the magnetosheath, 3) the magnetopause, 4) the magnetosphere, 5) the Northern tail lobe, 6) the Southern tail lobe, and 7) the Plasmasphere. The curved arrows represent deflected solar wind gas. Image Credit: NASA (Downloaded from Wikipedia.com)	13
Figure 2.2. Panel (a) shows the orientation of the planetary magnetic field, and panel (b) shows the ratio of the z component to the magnitude of the magnetic dipole moment vs its angle of inclination.....	14
Figure 2.3. Fractional difference between the derived and the assumed approximations to the planetary magnetic dipole moment.	21
Figure 3.1. Size comparison between several Solar System moons. The Earth is shown for reference. Image Credit: NASA (Downloaded from Wikipedia.com)	22
Figure 3.2. Surface features and internal structure of the Galilean moons. Image Credit: NASA/JPL	24

Figure 4.1. Summary of planetary radio emissions found in the Solar System. Taken from (Zarka, 1998).....	28
Figure 4.2. Jupiter-Io circuit diagram. The light green arrows over Io represent the current induced through the unipolar inductor mechanism.	31
Figure 4.3. Alfvén waves vs Magnetosonic waves.	33
Figure 4.4. P_s plotted as a function of r_s , keeping all other parameters constant, for prograde and retrograde orbits. Io's orbit and the synchronous orbit are shown for reference.	40
Figure 4.5. P_s plotted as a function of r_s for prograde orbits, and showing the radio power at each orbit compared to the maximum possible. Io's orbit and the synchronous orbit are shown for reference.	41
Figure 4.6. P_s plotted as a function of r_s , starting with values from the Jupiter-Io system and changing one parameter at a time. (a) $R_s = 2R_{Io}$, (b) $M_p = 2M_J$, (c) $\rho_s = 2\rho_{Io}$, (d) all Jupiter-Io values, (e) $T_p = 2 T_J$. The node seen at the synchronous orbit occurs because $V_p = 0$ at this orbital distance.	42
Figure 4.7. Radius of detectable exomoons in prograde and retrograde orbits for various flux sensitivities, for frequencies between 10 and 1000 MHz, and a plasma density of 10^5 amu/cm ³ . The distance to the system is set to 15 light years.	45
Figure 4.8. (a) Simulated dynamic spectra of typical Io-Jupiter arc emissions known as Io-A, Io-B, Io-C, and Io-D. The shade indicates the hemisphere from which the signal came, where black is for the Northern hemisphere and gray is for the Southern hemisphere [Taken from (Hess & Zarka, 2011)]. (b) Simulated dynamic spectra from an artificial Hot Jovian exoplanet with two orbital inclinations [Taken from (Hess & Zarka, 2011)]. Shade darkness represents relative intensity.	47

Figure 5.1. Io's plasma torus density profile shown as a function of distance from Jupiter between 6 and 10 R_J [Adapted from (Bagenal, 1994)]. The orbits of Io and Europa are shown for reference. Note: 1 amu/cm³ = 1.66×10⁻²¹ kg/m³, and 1 R_J = 69,911 km..... 49

Figure 5.2. Relative speed between the corotating plasma and a Jovian moon, V_p , for orbits between 1 and 10 R_J , expressed in Io units (1 unit ≈56.8 km/s). Io's orbit and Jupiter's boundary are shown for reference..... 51

Figure 5.3. Radio emission output power, P_S , calculated for various exomoon sizes in orbits between 6.5 and 10 R_J . The labels (P) and (R) denote prograde and retrograde configurations. We used the sizes of the Galilean satellites Europa, Io, and Ganymede as examples (labels E, I, and G respectively). All the moons used, as well as Earth's moon, L, are shown to scale for comparison. Power is given in Io units, where 1 unit ≈ 4.9 GW, as calculated by the model. 53

Figure 5.4. Four pathways through which an exomoon could become a detectable electromotive moon: (a) An exomoon using a hot Jupiter's magnetospheric plasma; (b) An exomoon which, like Io, provides enough plasma to create a dense torus; (c) An exomoon whose plasma torus is a combination of its own ionospheric plasma, and the plasma from a donor exomoon; and (d) An exomoon which relies solely on the plasma from one or more donor exomoons. The dashed curves are the field lines which connect the exomoons to the exoplanet's magnetic poles. Image Credit: Jupiter Photo NASA/JPL/Caltech (NASA photo # PIA00343)..... 57

Figure 6.1. Flux sensitivities (in Janskies) vs frequency for each of the four telescopes evaluated..... 59

Figure 6.2. Radii of exomoons potentially detectable with LWA and LOFAR..... 60

Figure 6.3. Position of all nearby stars within 15 light years from Earth, plotted in spherical coordinates. The size of the circle has a diameter of 20° , the color tells the star's distance from Earth, and the circle's outline tells how many stars are in the system (solid for singles, fine-dotted for binaries, and coarse-dotted for triples)..... 61

Figure 6.4. Radii of exomoons potentially detectable with GMRT..... 62

Figure 6.5. Targets proposed to GMRT. Targets inside the blue squares are observed targets. The Arecibo declination limit is shown as a comparison to the GMRT declination limit..... 63

Figure 6.6. Preliminary results from the GMRT target Epsilon Eridani..... 63

Figure 6.7. Radii of exomoons potentially detectable with SKA. 64

Figure 7.1. Interactions between radio emissions powered by an electromotive moon (a) with secondary moons. Exomoon (c) is occulting the radio signal, while exomoon (b) is reflecting and polarizing the signal, and exomoon (d) is a non-interacting moon. 67

Chapter 1

Introduction

Since the discovery of the first extra-solar planet around the pulsar PSR1257+12 using Arecibo Observatory observations (Wolszczan & Frail, 1992), and the discovery of the first exoplanet around a Sun-like star (Mayor & Queloz, 1995), the field of exoplanet detection has been through a great deal of development in techniques and instrumentation. Various ground-based and space-based surveys have led to the confirmation of over 1900 exoplanets¹, and thousands of exoplanet candidates identified by NASA's *Kepler*² space telescope.

Based on the structure and history of our own solar system, one might expect extra-solar moons (exomoons) to be at least as common as exoplanets. After all, moons in our solar system far outnumber planets. In fact, as of the writing of this work, there are at least 146 confirmed moons in our solar system, plus another 27 awaiting official confirmation.³ Two of these moons, Ganymede (of Jupiter) and Titan (of Saturn), are so large that they are even larger than the planet Mercury.

Despite the progress and the favorable statistics, the current limits of observational techniques have not made it possible to confirm any exomoon. There are currently two known exomoon candidates awaiting independent verification (see Chapter 6), but due to the nature of the observations one will take a long time to be verified, and the other one may never be verified at all. The seemingly insurmountable challenges of finding exomoons are precisely what motivated us to take a different approach, and propose the use of radio rather than optical frequencies to search for them.

¹ <http://exoplanet.eu/catalog/>

² <http://kepler.nasa.gov/Mission/discoveries/candidates/>

³ <https://solarsystem.nasa.gov/planets/profile.cfm?Display=Moons>

In this chapter I will present an overview of exoplanet detection techniques, and their results. First, I will present the two most successful techniques, the transit and radial velocity methods, followed by a discussion on radio detection, and a summary of a few other detection techniques available. Finally, I will discuss discoveries made so far up until the time of this writing, and where planetary research may be headed in the near future.

1.1 The Transit Method

An exoplanet transit occurs when an exoplanet passes in front of its star, as seen from Earth, creating a tiny eclipse that temporarily dims the star's light by a tiny fraction. For a transit to be visible, the star, the Earth, and the orbit of the planet need to be aligned to within a very small angle, which means that only a small percentage of exoplanets can be discovered by this method. The fact that so many exoplanets have been discovered by this technique (see Figure 1.5), gives us a good sense of just how numerous planets really are. On Figure 1.1(a), we can see a simplified diagram showing the different stages of a transit. At t_I on the figure, the planet begins to block the star (the *ingress*), and so the *flux* of light from the star begins to diminish. At t_{II} the entire disc of the planet is in front of the star, at this point the maximum decrease in flux, δ , is reached. In this simplified version, the flux remains at its minimum until the planet's disc begins to exit the disc of the star (the *egress*) at time t_{III} . The egress of the planet lasts from t_{III} to t_{IV} , at which point the star's flux returns to normal values.

The diagram on Figure 1.1(a) also shows a parameter 'b' known as the impact parameter, which measures how far from the center of the star the transit occurs. In other words, the impact parameter tells us the length of planet's closest approach (from the planet's center) to the center of the star during its transit. If b plus the planet's radius is

smaller than the star's radius, then the transit is a *full* transit, otherwise it is a *grazing* transit. Whether we see a transit as full or grazing depends largely on the angle between our line of sight to the star and the orbital plane of the planet.

Another characteristic of transits that is ignored by Figure 1.1(a) is the fact that planets do reflect some of the light they get from their star. Just like the moon illuminates the night sky by different amounts at different phases, the amount of reflected light that the planet contributes to the total flux depends on the position of the planet in its orbit. When the planet transits, its night side points towards Earth, so it does not contribute any light, rather it blocks the light from the star so we get a dip in the total flux. When the planet is to the side of the star some of its dayside light contributes to the star's light, especially towards the far side of its orbit where most of its dayside is visible. As the planet hides behind its star, however, all the light from its dayside is blocked by the star and we get a secondary transit. Additionally, the star's light is not uniform through the cross-section of the star, but the star in fact becomes darker towards the edge. This phenomenon is called *limb darkening*, and it makes the bottom of the light curve rounded instead of flat.

When all the physical effects and observational noise are taken into account, we get a curve like the one shown on Figure 1.1(c), which is the real curve of the planet Kepler 444e, as observed by the Kepler telescope.

On Figure 1.1 we can also see examples of transits that were readily visible from Earth. The first transit, shown on panel (e), is the transit of Venus that took place June 5th, 2012, and it is an example of a full transit. The second transit, shown on panel (f), is actually a partial lunar eclipse that occurred on October 23rd, 2014, and it is an example of a grazing transit.

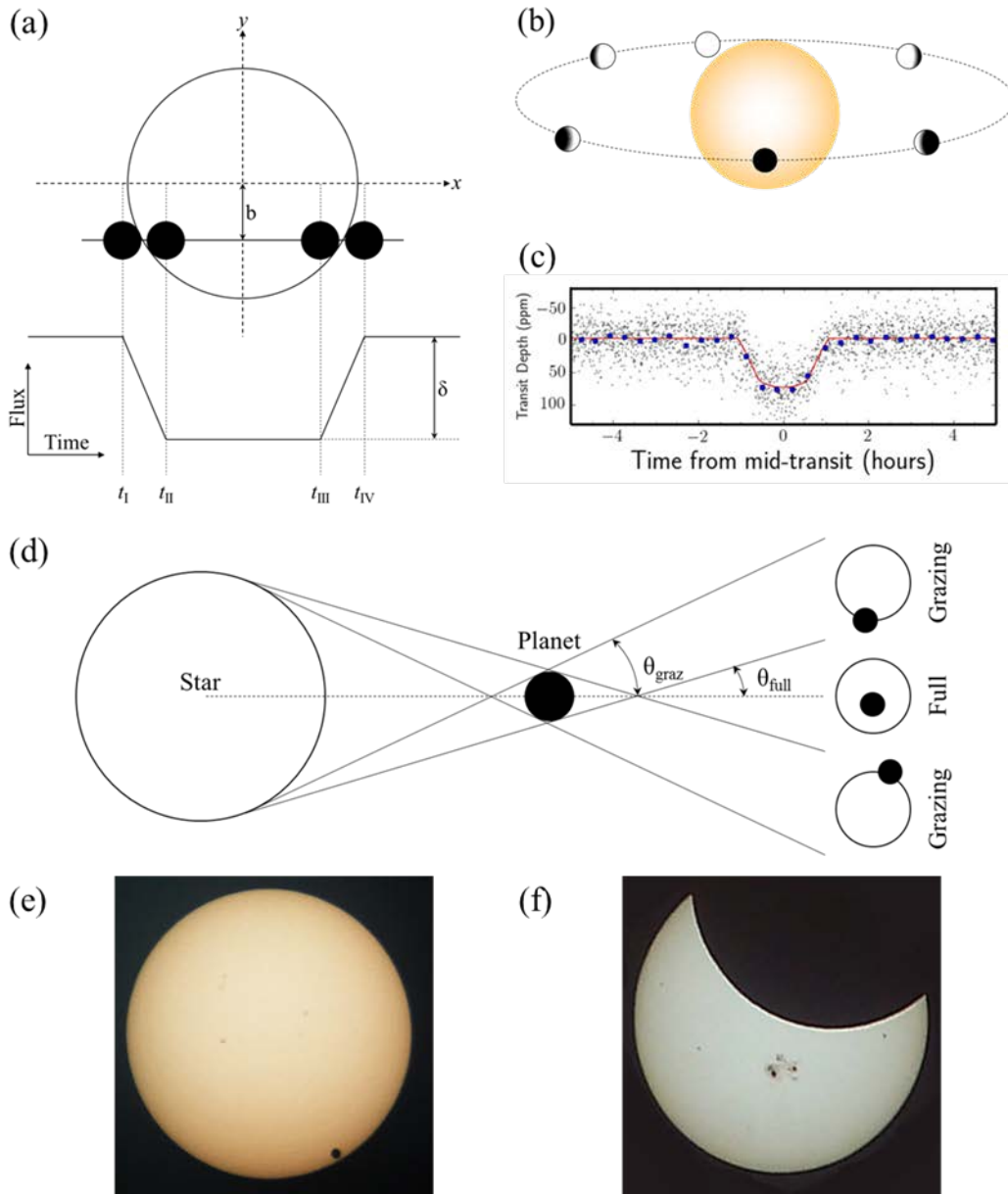


Figure 1.1. Properties and examples of transit events. Panel (c) taken from (Campante, et al., 2015). Other Image Credits: panel (e) Suman Satyal, panel (f) Billy Quarles.

1.2 The Radial Velocity Method

The Radial Velocity detection method, (RV), is based on the *Doppler Shift*, which is a change on the observed wavelength of light due to the motion of the source. RV works by taking advantage of the fact that massive objects orbit around the center of mass of the system, which means even the most massive objects in the system will still appear to wobble. Hence, exoplanets will make their stars wobble around the common center of mass, and this wobble is what causes a Doppler shift in the star light's wavelength. This shift will make the wavelength smaller (blue shifted) when the star is moving towards us, and larger (red shifted) when moving away from us (see Figure 1.2). RV has been very successful, helping to identify hundreds of exoplanets to date.

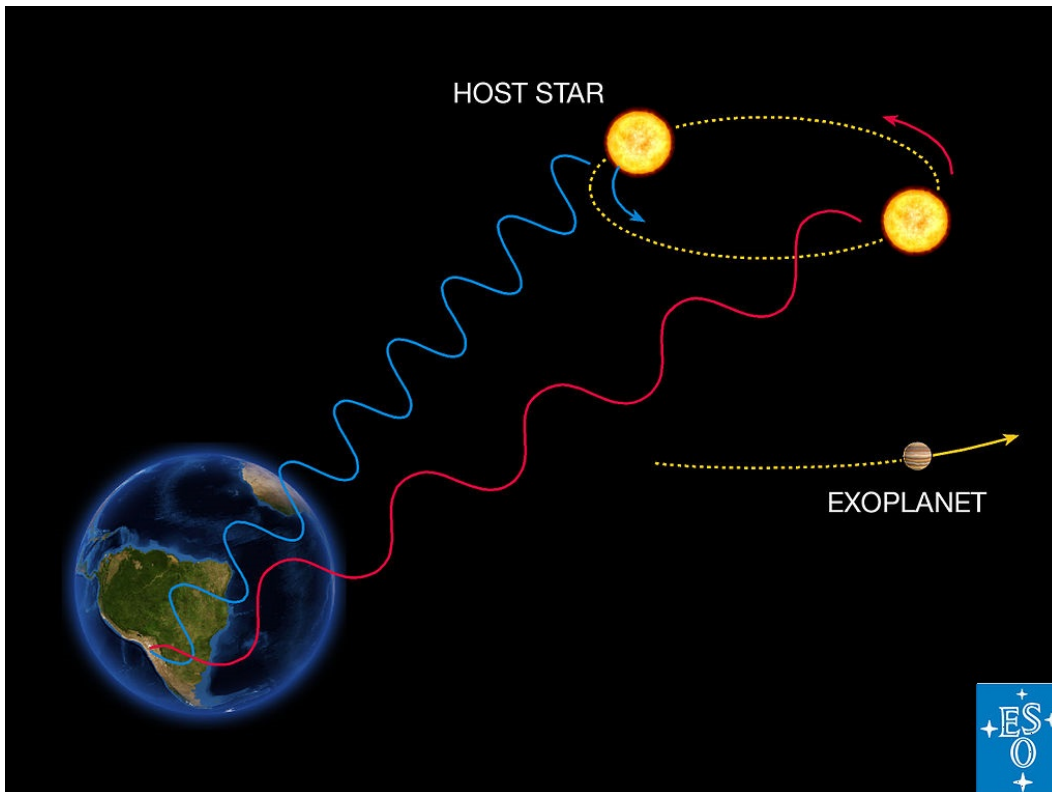


Figure 1.2. Radial velocity diagram. The exoplanet causes the star to wobble around the center of mass, which in turn causes a Doppler shift in the star light's wavelength.

1.3 Radio Detection

Jupiter is the strongest radio emitter in the solar system (Su, 2009). Some of those radio emissions are caused by the Galilean moons like Io, and others by either the solar wind or the plasma from Jupiter's ionosphere. The latter two types are collectively called *auroral* radio emissions, and only those with frequencies larger than about 3 MHz are visible by ground radio telescopes. The moon Io also produces strong radio emissions above 3 MHz, and are referred to as *Io-DAM* (i.e. decametric wavelengths), and so auroral radio emissions at those wavelengths have become known as *non-Io-DAM*. There are several studies that suggest exoplanets can be detected through radio emissions analogous to Jupiter's non-Io-DAM (Nichols, 2011); (Zarka, 2007). In particular, Jonathan Nichols hypothesized that the magnetosphere–ionosphere coupling mechanism seen on Jupiter could also occur on giant exoplanets, and produce powerful enough radio emissions to be detectable from Earth (Nichols, 2011). The emission process described by Nichols and the process presented in this dissertation are both based on the unipolar inductor mechanism, and their plasma source is the moon Io. However, the circuit made by the current in each case is fundamentally different. In our study, the circuit directly couples Io to Jupiter's poles, whereas in Nichols's study, the current bypasses Io and instead flows through magnetic field lines well beyond the moon. Consequently, the signal produced by each process is very different, and easily distinguishable from the other.

Auroral radio emissions require a large stellar luminosity. Specifically, they require large X-ray and EUV stellar irradiation of the exoplanet's ionosphere to produce a detectable radio signal. In other words, this detection technique has the same bias as the radial velocity and transit techniques mentioned previously. Our detection method, as

explained in this dissertation, does not have such a bias, and in fact favors low stellar irradiation scenarios. More importantly, in the case of magnetosphere-ionosphere coupling, Nichols emphasizes active moons as possible sources of plasma, but this might not be the case. Recent computational studies have shown that stellar irradiation alone can ionize the hydrogen-rich atmosphere of a Jovian exoplanets to levels that can match and even vastly exceed the amount of plasma in Io's plasma torus (Koskinen, et al., 2010). In other words, Nichols's mechanism cannot be used to detect exomoons, only exoplanets.

Ultimately, radio telescopes have not found any exoplanet to date, in spite of the many searches done with several radio telescopes, but the search continues (Winterhalter, et al., 2015).

1.4 Other Detection Techniques

Gravitational microlensing and direct imaging are two other techniques that have yielded good results. There is also a class of techniques called timing variations, which have yielded some discoveries by taking advantage of temporal changes in the observation of an event (like a transit) caused by a planet to infer its existence. Other techniques have been suggested, like astrometry and orbital brightness modulation, but those techniques have either yielded only a few detections or none at all.

In gravitational microlensing, when a star (or another massive object) passes in front a light source it bends the light from that source, making it brighter to the observer for a short amount of time. If that star has an exoplanet, the exoplanet will also cause the background light to brighten, although by a smaller amount and at a slightly different time (see Figure 1.3). This method can detect exoplanets which are relatively far away (even thousands of light years), and favors more massive exoplanets. A big disadvantage of

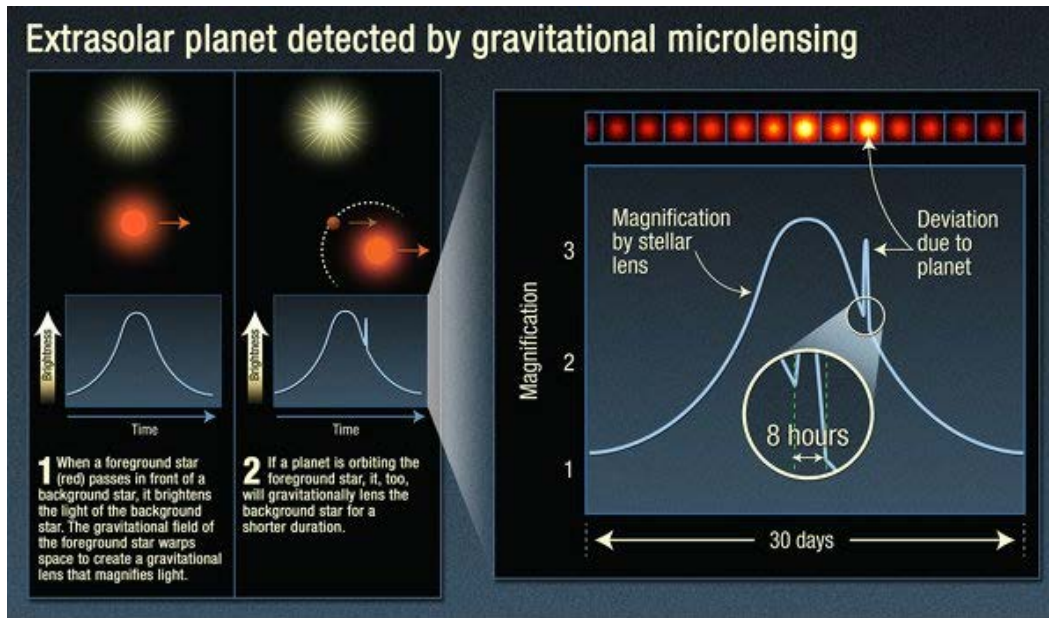


Figure 1.3. Gravitational microlensing by an exoplanet. © NASA, ESA, and A. Feild (STScI)

microlensing, however, is that it relies on the near-alignment of the exoplanet and the background light source, so each exoplanet is unlikely to be observed more than once.

In the case of timing variations, an exoplanets can be discovered by measuring the changes it induces in the period of the transits of a previously known exoplanet. Timing variations can also be used with pulsars. Pulsars are rapidly rotating neutron stars that emit intense radio waves, which can be detected on Earth. Signals from pulsars have very precise timing, so the regular deviations from this timing caused by the mass of an orbiting exoplanet can be measured, thereby detecting the exoplanet. The intensity of the variations on transit and pulsar timing is proportional to the gravitational force of exoplanet causing them, so larger exoplanets with smaller orbits are easier to detect.

Direct imaging of exoplanets is accomplished by blocking the light from the host star with a *coronagraph*, and accumulating the dim light from exoplanets. This technique is naturally biased towards younger (hotter) planetary systems, and currently it has only

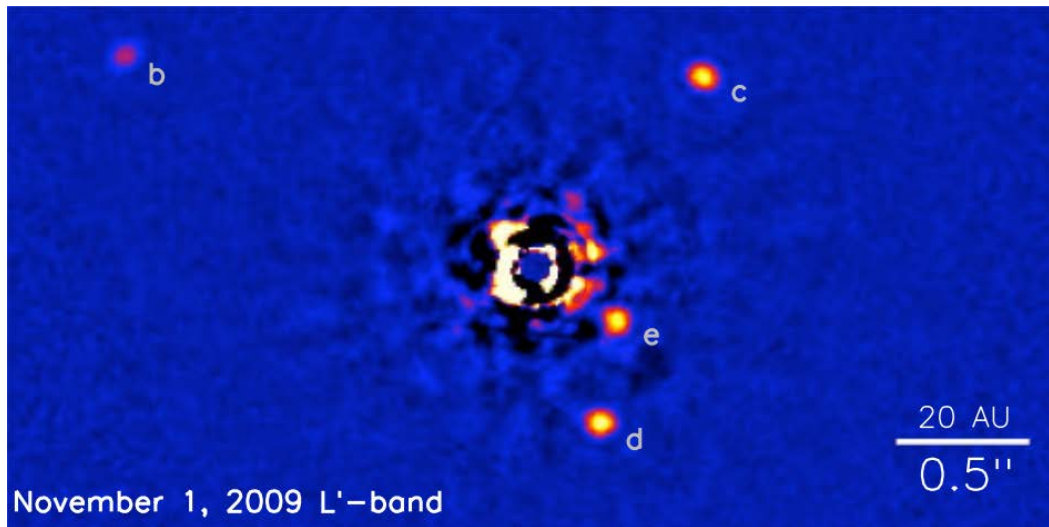


Figure 1.4. Direct Imaging of HR 8799bcde at 24, 38, 68, and 14.5 AU; ~39pc from Earth (~127 ly). Using Keck & Gemini. Taken from (Marois, et al., 2010).

been possible to observe exoplanets that are far away from their star, like the HR 8799 system shown on Figure 1.4 (Marois, et al., 2010).

For a more comprehensive review of current exoplanet detection techniques, please refer to (Seager, 2010).

1.5 Exoplanet Statistics

Over 1900 exoplanets have been confirmed to this day. The most successful instrument in searching for exoplanets is NASA's Kepler telescope using the transit method. As far as techniques are concerned, the radial velocity method was the most successful technique until 2014, when the transit method surpassed it. Because RV and the transit method have been the most successful, there is a large bias in the kind of exoplanets that can be found. Specifically, Jupiter-like gas giants with small orbits are by far the most represented in today's exoplanet catalogs (see Figure 1.5). Nevertheless, exoplanets just slightly bigger than Earth are becoming more common, as are exoplanets in larger orbits, including some in the so called *habitable zone*.

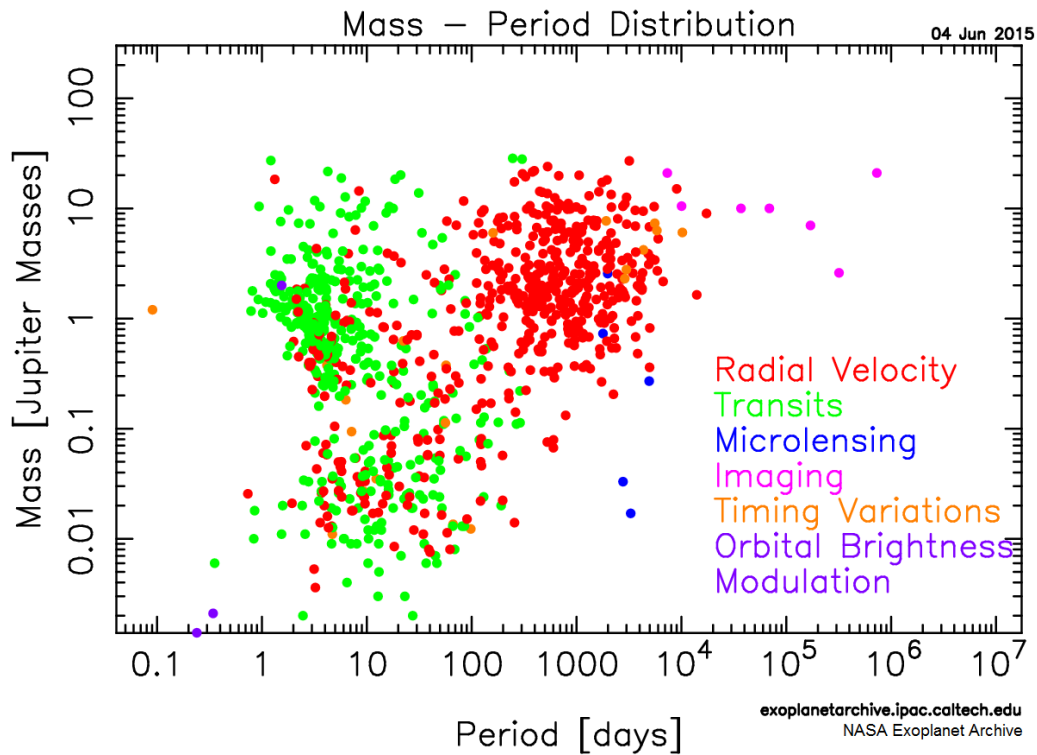


Figure 1.5. Mass and period distribution of all confirmed exoplanets, color coded by their detection method.

1.6 The New Frontier

In spite of all the progress made, and all the exoplanets discovered, there has not been a single exoplanetary moon (exomoon) discovery. Inspired by this, my collaborators and I designed a detection technique using radio waves rather than visible light, and which could potentially do what nobody has been able to do: confirm the existence of exomoons.

To explain this new technique, I will begin by presenting some background information and assumptions, then I will explain the theory behind it and its predictions. Finally I will cover the progress made towards searching for signals with radio telescopes.

Chapter 2

Planetary Magnetospheres

Many bodies in the Solar System, including Earth and the gas giants, have magnetic fields that interact with the solar wind and other plasmas. The area where the magnetic field dominates the behavior of the plasmas in it is known as a *magnetosphere*. Consequently, one can expect exoplanets to have similar magnetic fields and magnetospheres. In this chapter I will review the structure of said magnetospheres, and describe the model I use to approximate the planetary magnetic field, which will be used to calculate radio emission power in later chapters.

2.1 Magnetosphere Topology

There are various examples of magnetospheres in our Solar System. Some, like on Earth and Jupiter, are produced by the presence of a permanent planetary magnetic field affecting the flow of solar and planetary plasma around a body. Such magnetospheres are called *intrinsic* magnetospheres. Others, like in the case of Mercury and Venus, are induced by the deflection of the magnetized solar wind by an unmagnetized body (Kallenrode, 2004). Mathematically, if the distance (from the exoplanet) at which the stellar wind pressure and the magnetic field pressure are equal is much larger than the planetary radius, then the magnetosphere is intrinsic, otherwise it is induced. This distance is also referred to as the *stand-off* distance, or *Chapman-Ferraro* distance. To find the stand-off distance, we start with the definition outlined before, as shown in Equation (2.1).

$$\frac{1}{2} \rho_{sw} V_{sw}^2 = \frac{1}{2} \frac{B^2}{\mu_0}. \quad (2.1)$$

In Equation (2.1), the ρ_{sw} and V_{sw} are the stellar wind's density and velocity, and B is the planetary magnetic field. One can solve that equation for B , and then use Equation (2.6) to solve for the Chapman-Ferraro distance, r_{CF} , which yields

$$r_{CF} = \left(\frac{B_{Surf}^2 R_p^6}{\mu_0 \rho_{sw} V_{sw}^2} \right)^{\frac{1}{6}}, \quad (2.2)$$

where B_{Surf} is the magnetic field at the exoplanet's equator, and R_p is the planetary radius. Earth and the four giant planets have intrinsic magnetospheres with stand-off distances of over 10 planetary radii, with Jupiter's having the largest one at 47 – 97 R_j (Kallenrode, 2004). Intrinsic magnetospheres are the only kind that are relevant to this work, thus I will refer only to that type of magnetospheres from this point forward.

The interaction between magnetic field and stellar wind creates an outermost layer called the **bow shock** (shown as label 1 in Figure 2.1), and it is the place where the stellar wind slows down from supersonic to subsonic speeds as it encounters the planetary magnetic field. It has been suggested that bow shock observations during transits could allow us to detect and measure that magnetic field of exoplanets for the first time (Vidotto, et al., 2011). Next is the **magnetosheath** (label 2), which serves as a transition layer between the bow shock and the magnetopause, and contains mostly shocked stellar wind and a small portion of magnetospheric plasma. Stellar wind gas collects and thermalizes in the magnetosheath, which causes it to have high energy particle energy flux, and causes the magnetic field to change erratically in both magnitude and direction. (Kallenrode, 2004)

The **magnetopause** (label 3) is the layer where the stellar wind pressure exactly balances the magnetic field pressure. The stand-off distance estimated by Equation (2.2)

gives only the distance from the center of the planet to the magnetopause along the line between the planet and the sun (or exoplanet and star), the distance to the magnetopause is different in other directions due to the asymmetries cause by the stellar

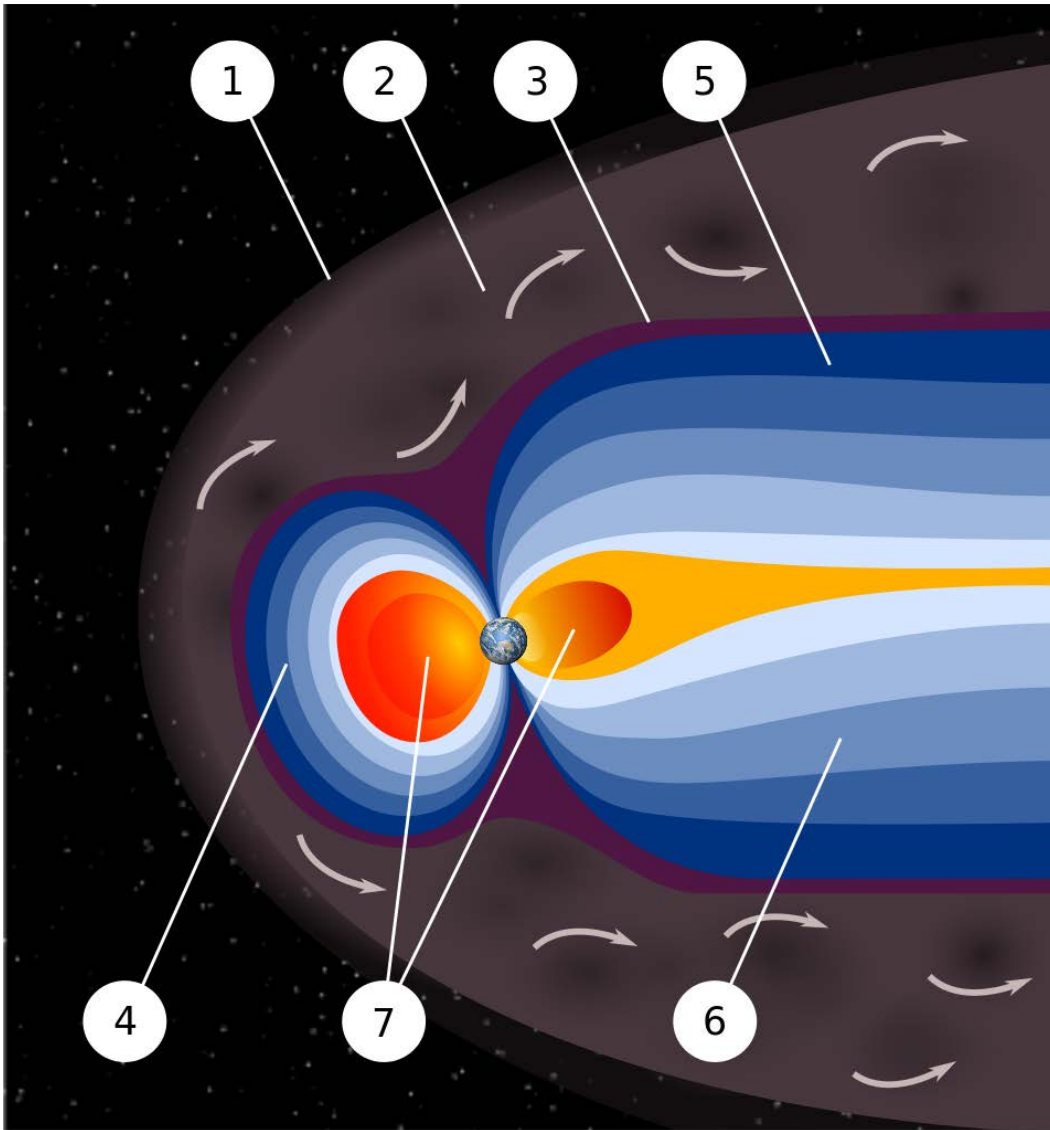


Figure 2.1. Structure of a magnetosphere with its major parts labeled. The major parts are 1) the bowshock, 2) the magnetosheath, 3) the magnetopause, 4) the magnetosphere, 5) the Northern tail lobe, 6) the Southern tail lobe, and 7) the Plasmasphere. The curved arrows represent deflected solar wind gas. Image Credit: NASA (Downloaded from Wikipedia.com)

wind and the dipolar nature of the magnetic field (Kallenrode, 2004).

Once inside the magnetopause boundary, the magnetic field of the planet becomes the dominant force controlling the plasmas present in the region, and thus we have officially arrived at the **magnetosphere** (label 4). As we can see from Figure 2.1, the side of the magnetic field facing the exoplanet's star is compressed by the stellar wind pressure, whereas the opposite is extended. The extended side of the magnetosphere, on the opposite side to the star is known as the **magnetotail**, and has two main lobes: the **Northern** tail lobe, which points towards the exoplanet, and the **Southern** tail lobe, which points away from the exoplanet. The magnetotail extends far behind the planet, in the case of Jupiter extending all the way to the orbit of Saturn! (Kallenrode, 2004).

Finally, the **plasmasphere** is a donut-shaped region around the exoplanet where the dominant plasma is cool, and low density (Kallenrode, 2004). The source of this plasma varies from case to case, but for Jupiter the majority of the plasma comes from Io's volcanism (Lopes & Spencer, 2007).

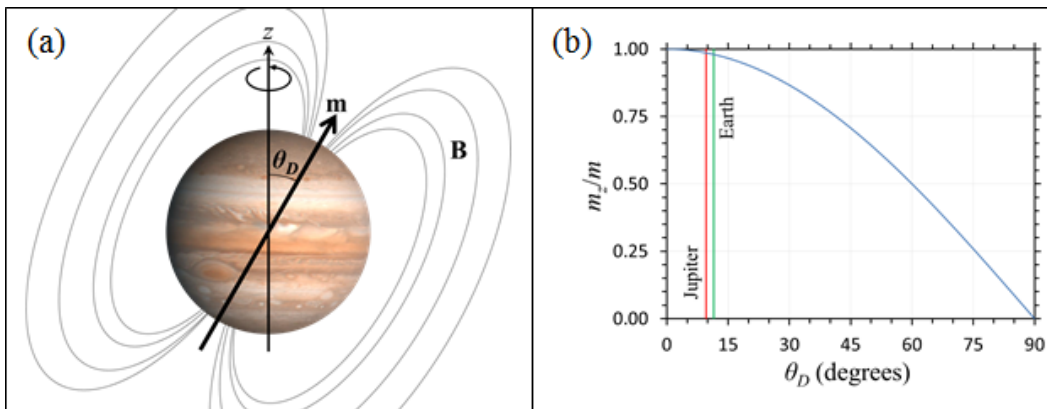


Figure 2.2. Panel (a) shows the orientation of the planetary magnetic field, and panel (b) shows the ratio of the z component to the magnitude of the magnetic dipole moment vs its angle of inclination.

Now that we have identified the main components created by the interaction between stellar winds and planetary magnetic fields, the next step is to find a good analytical model for this magnetic field that can be used in the theory that follows.

2.2 Modeling Planetary Magnetic Fields

To model an exoplanet's magnetic field, we begin by assuming that the field is mostly dipolar, as is approximately the case for all magnetized bodies in the solar system, and describe the field in terms of its magnetic dipole moment, \mathbf{m}_p . For a planet rotating around the z-axis with a period of T_p , and an angular velocity $\omega_p = 2\pi/T_p$, the magnetic dipole moment can be described by

$$\mathbf{m}_p(\mathbf{r}) = m_p \begin{pmatrix} \sin \theta_D \cos \omega_p t \\ \sin \theta_D \sin \omega_p t \\ \cos \theta_D \end{pmatrix}, \quad (2.3)$$

where m_p is the magnitude of the magnetic moment, and θ_D is its inclination with respect to the z-axis. Figure 2.2(a) illustrates the geometry of this quantities. When Equation (2.3) is averaged over one planetary revolution, the x and y components vanish, so the average magnetic dipole moment felt by objects near the planet is

$$\mathbf{m}_p(\mathbf{r}) = m_p \cos \theta_D \hat{\mathbf{z}}. \quad (2.4)$$

From Figure 2.2(b) we can see that the the x and y components of m are negligible even for fairly large θ_D and, as shown in Figure 2.2(b), Earth and Jupiter are clear examples of this. Therefore, from now on I will assume that $\mathbf{m}_p \approx m\hat{\mathbf{z}}$.

The magnetic field due to a dipole moment is given by

$$\mathbf{B}(\mathbf{r}) = \frac{\mu_0}{4\pi} \left[\frac{3(\mathbf{m}_p \cdot \hat{\mathbf{r}})\hat{\mathbf{r}} - \mathbf{m}_p}{r^3} \right]. \quad (2.5)$$

Using the approximation for the magnetic dipole moment, (2.5) becomes

$$\mathbf{B}(\mathbf{r}) = \frac{\mu_0}{4\pi} \frac{m_p}{r^3} [3(\hat{\mathbf{z}} \cdot \hat{\mathbf{r}})\hat{\mathbf{r}} - \hat{\mathbf{z}}], \quad (2.6)$$

After performing the dot product and trigonometric manipulations, the magnitude of the magnetic field, in spherical coordinates, is found to be

$$B(\mathbf{r}) = \frac{\mu_0}{4\pi} \frac{m_p}{r^3} (3\cos^2 \theta + 1)^{\frac{1}{2}}. \quad (2.7)$$

This equation gives as the magnitude of the magnetic field at any point in space, but what is needed is to be able to track B at any point within a *specific* field line, i.e. the field line that connects exomoons to their exoplanet. To achieve this goal, I can make use of a field line's relationship between radial distance and polar angle, which is given in Equation (2.8). I have taken an exomoon's orbital radius, r_s , to be the scale reference because this scale will be very useful in later chapters. Additionally, the exomoon used for reference is assumed to orbit around the exoplanet's equatorial plane

$$r = r_s \sin^2 \theta. \quad (2.8)$$

Using the trigonometric identity $\sin^2 \theta + \cos^2 \theta = 1$ with Equation (2.11) yields

$$\cos^2 \theta = 1 - \frac{r}{r_s}, \quad (2.9)$$

which can now be substituted into Equation (2.7) to get

$$B(r) = \frac{\mu_0}{4\pi} \frac{m_p}{r^3} \left(4 - 3 \frac{r}{r_s} \right)^{\frac{1}{2}}, \quad (2.10)$$

thereby eliminating the θ dependence from the magnetic field equation.

As mentioned before, my purpose was to derive an equation that could allow me to tract the magnetic field through a given field line, and Equation (2.10) fulfills that

purpose well. However, if I only need to know the magnetic field felt by exomoons orbiting near the rotational equator, I can find that right away from Equation (2.5) by setting $\mathbf{m}_p = m\hat{\mathbf{z}}$, to get

$$B_S = \frac{\mu_0}{4\pi} \frac{m_p}{r_S^3}. \quad (2.11)$$

Now that I have an equation describing the magnetic field, I can proceed to find a good approximation for the magnetic dipole moment. Authors who studied the planetary radio emissions often use an empirical approximation known as Blackett's Law to obtain the planetary magnetic dipole moment (Joseph, et al., 2004). As shown in Equation (2.12), Blackett's law states that the magnetic moment, m , of a gas giant depends on a power of its angular velocity, k , and a power of its mass, l . Common values for k and l are 1 and 2, respectively, although other values have also been used (Lazio, et al., 2004).

$$m_p \propto \omega_p^k M_p^l. \quad (2.12)$$

This approximation works fairly well for the giant planets in the Solar System, but for my calculations I opted to use a model that can be at least partially justified using standard electrodynamics (Durand-Manterola, 2009). In this approximation, the magnetic moment of a planetary body can be expressed as

$$m_p = 10^{-5} \left(\frac{\sigma M_p}{T_p} \right)^K, \quad (2.13)$$

where M_p and T_p are the exoplanet's mass and rotation period, K is experimentally set to 1.15 (Noyola, et al., 2014), and σ is the conductivity of the liquid at its core, which is responsible for creating the magnetic field. In the case of giant planets, the liquid that creates their magnetic field is metallic hydrogen, which is estimated to have a

conductivity of about $2 \pm 0.5 \times 10^5$ S/m (Shvets, 2007), which is on the same order as that of graphite's conductivity along the basal plane (Pierson, 1993). As a point of comparison, the conductivity of metal is on the order of 10^7 - 10^8 S/m. For convenience, m_p can also be expressed in Jupiter units as

$$m_p = m_J \left(\frac{M_p T_J}{M_J T_p} \right)^K, \quad (2.14)$$

where m_J is Jupiter's magnetic dipole moment (1.56×10^{27} Am²), M_J is Jupiter's mass (1.8986×10^{27} kg), and T_p is Jupiter's rotation period (9.925 hours).

The model assumes that the exoplanetary magnetic field rotates at the same rate as the exoplanet, as is the case for Jupiter and the other planets, and that the rotation period, T_p , is also the same as Jupiter's. How to predict the spin rate of planets is still an open debate in planet formation theory, but currently the most accurate fit to the observational data is one of a linear relationship between $\log(M_p)$ and the log of a planet's spin angular momentum (Hughes, 2003). In other words, it would not be unreasonable to assume that bigger M_p means smaller T_p , especially after β Pictoris b's rotation period was found to be $\approx 8.1 \pm 1.0$ hours (Snellen, et al., 2014) or $\approx 18\%$ faster than Jupiter. Additionally, we can see from Equation (2.14) that a smaller period leads to a larger magnetic moment, which in turn leads to a larger B_s , and thus a higher emission power P_s . Therefore, assuming that $T_p = T_J$ is a conservative assumption, and should work well for our purposes.

The expression for the magnetic field affecting the exomoon is then

$$B_S = \frac{10^{-12}}{r_S^3} \left(\frac{\sigma M_P}{T_P} \right)^K = 10^{-7} \frac{m_J}{r_S^3} \left(\frac{M_P}{M_J} \right)^K, \quad (2.15)$$

and thus we now have an expression for the magnetic field felt by the exomoon which depends only on the planetary mass and the exomoon's orbital radius.

2.3 Magnetic Dipole Moment Approximation

To justify the approximation used in Equation (2.13), I can begin by considering a dipole magnetic field with $\mathbf{m}_p = m\hat{\mathbf{z}}$, just like before, and assume that there are no contributing currents outside the exoplanet's core. This latter assumption means that $\nabla \times \mathbf{B} = 0$, so I can find the magnetic scalar potential. For a dipole seen from a distance \mathbf{r} , the magnetic scalar potential Ψ is given by (Jackson, 1999, p. 196)

$$\Psi(\mathbf{r}) = \frac{\mathbf{m}_p \cdot \mathbf{r}}{4\pi r^3} = \frac{m_p \cos \theta}{4\pi r^2}. \quad (2.16)$$

Similarly, the magnetic scalar potential for any closed current loop as seen from a distance is

$$\Psi(\mathbf{r}) = -\frac{\mu_0}{4\pi} I \Omega, \quad (2.17)$$

where I is the current, and Ω is the solid angle subtended by the loop. Combining Equations (2.16) and (2.17), and solving for m_p we get

$$m_p = -\mu_0 I \Omega r^2 \sec \theta. \quad (2.18)$$

Since the exomoons that will be discussed later orbit on, or very close to, the equatorial plane, I can exclude non-equatorial planes and set $\theta = 0$. Next, I can use Ohm's law to express I in terms of the conductance, Σ , and the electromotive force, \mathcal{E} , which gives

$$m_p = -\mu_0 \Sigma \mathcal{E} \Omega r^2. \quad (2.19)$$

Next, I can use Faraday's Law of Induction, and the chain rule to derive the expression

$$\mathcal{E} = -\frac{d\Phi_B}{dt} = -\frac{d\Phi_B}{d\phi} \frac{d\phi}{dt} = -\frac{2\pi}{T_p} \frac{d\Phi_B}{d\phi}. \quad (2.20)$$

Now Equation (2.19) becomes

$$m_p = \frac{2\pi\mu_0 \Sigma \Omega}{T_p} \frac{d\Phi_B}{d\phi} r^2. \quad (2.21)$$

If I set $r = R_p$, then the conductivity of the circuit is $\sigma = \Sigma / (2\pi R_p)$, and m_p can now be expressed as

$$m_p = \frac{3\pi\mu_0 \sigma \Omega}{T_p} \frac{d\Phi_B}{d\phi} \left(\frac{4\pi}{3} R_p^3 \right). \quad (2.22)$$

The term in the parenthesis is simply the volume of the exoplanet, which is the mass of the exoplanet, M_p , divided by its average density, ρ_p . Using this definition to eliminate R_p , and rearranging the variables I get

$$m_p = \left(\frac{3\pi\mu_0 \Omega}{\rho_p} \frac{d\Phi_B}{d\phi} \right) \frac{\sigma M_p}{T_p}. \quad (2.23)$$

In other words, if I assume the terms in parenthesis to be a proportionality constant (zeroth order approximation), then I am left with the conclusion that

$$m_p \propto \frac{\sigma M_p}{T_p}, \quad (2.24)$$

which only differs from the original approximation in that the exponent is 1 rather than 1.15. Since we are assuming that exoplanets rotate at about the same rate as Jupiter, then the difference between the two approximations is

$$\frac{m_p(K = 1.15)}{m_p(K = 1)} = \left(\frac{M_p}{M_J} \right)^{0.15} . \quad (2.25)$$

Plotting Equation (2.25) for exoplanet masses between 1 and 10 M_J yields Figure 2.3, which shows that even for an exoplanet as big as 10 M_J , the difference between approximations is only about 40%, validating the derivation.

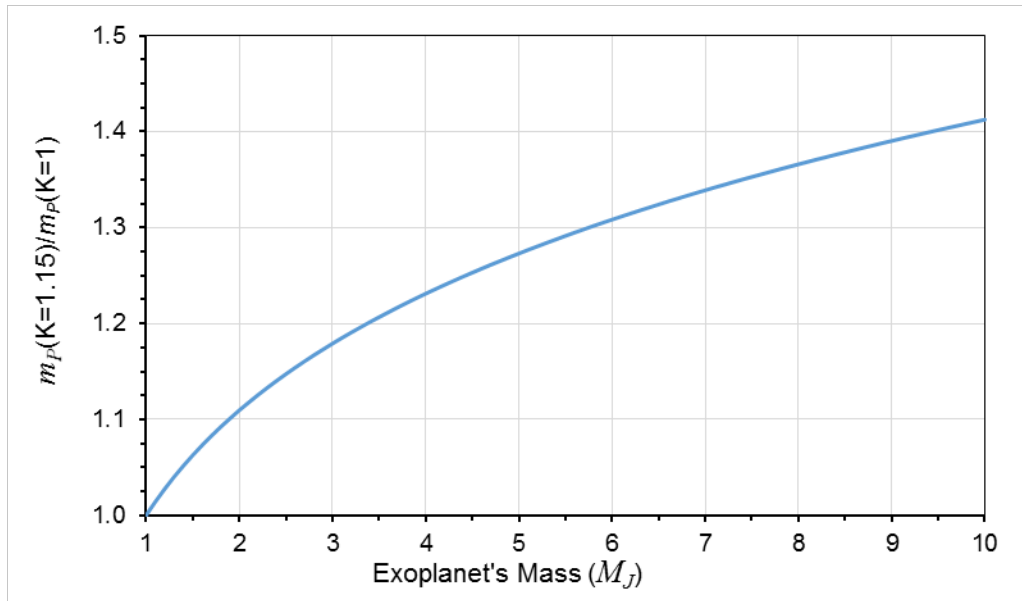


Figure 2.3. Fractional difference between the derived and the assumed approximations to the planetary magnetic dipole moment.

Moons are also classified by the type of orbit they occupy. All large moons in our solar system have near circular orbits on a plane very close to the plane of their planet's equator. Small moons, especially irregular moons, can have very elliptical orbits (called *eccentric* orbits), which deviate significantly from the planet's equator (referred to as *highly inclined* orbits). An important characteristic of a moon is whether its orbital motion is *prograde*, in the same direction as the rotation of its planet, or *retrograde*, opposite to the planet's direction of rotation. All large moons except for Neptune's Triton have prograde orbits, which has some important consequences for my model, as will be explained in the next chapter.

3.1 Io and the Galilean Moons

Jupiter has over 60 moons identified to date, but only four of them are major satellites: Io, Europa, Ganymede, and Callisto. These moons are massive, with the largest moon Ganymede being larger than the planet Mercury. Together they are known as the *Galilean Moons* because they were discovered by Galileo Galilei around 1610 after improving his telescope (Galilei, 1989). Looking at Figure 3.1 one can really appreciate just how massive and varied the Galilean moons are, with only Titan and Earth being comparatively noticeable in the picture.

The Galilean moons are rich in geographical and structural features. Io, for example, is an intensely volcanic moon that creates a light atmosphere of SO₂ around Io, which then ionizes to create an ionosphere, and a toroidal plasma structure around Jupiter referred to as a plasma torus (Lopes & Spencer, 2007). Then there is Europa with a severely cracked icy surface, and which has long been suspected to have a subsurface ocean. In fact, all of the Galilean moons but Io are suspected to have subsurface oceans. Ganymede is so large that it has its own intrinsic magnetic field, and finally Callisto whose internal structure seems to be only partially differentiated despite being almost as

large as Ganymede. Figure 3.2 has images of the Galilean moon surfaces, as well as a diagram showing the internal structure as it is currently understood.

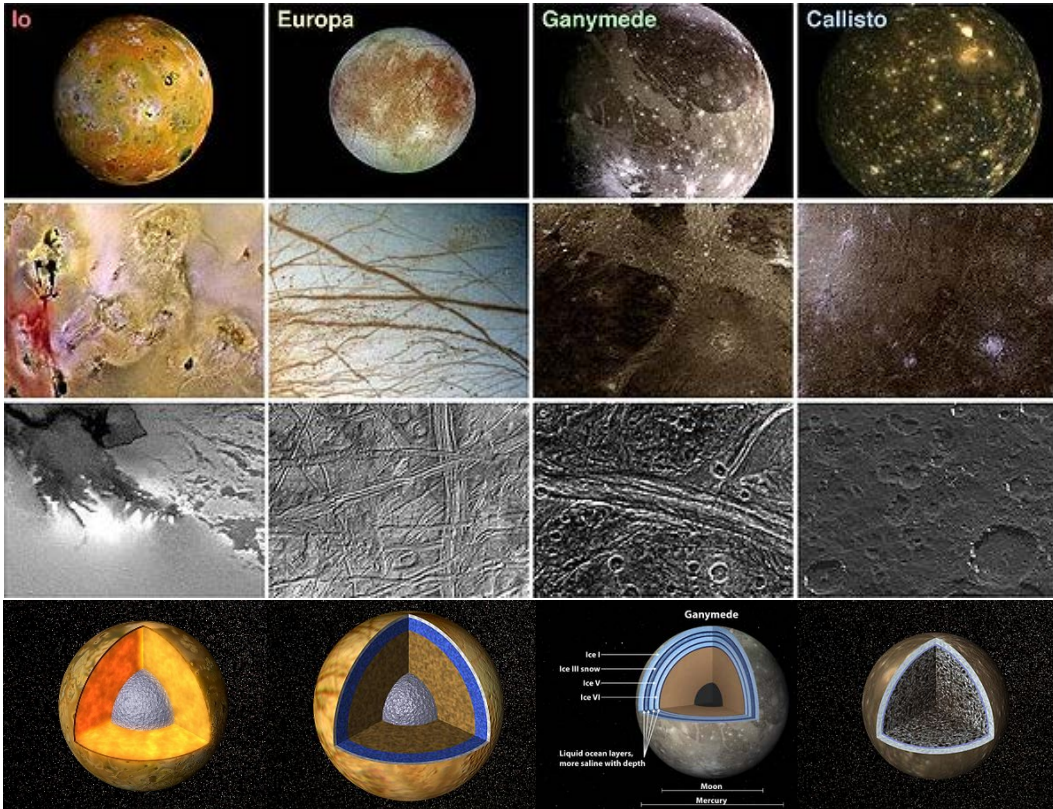


Figure 3.2. Surface features and internal structure of the Galilean moons. Image Credit: NASA/JPL.

3.2 Notes on Moon Formation

Radio detection favors large exomoons, as I shall explain later. The power of satellite-related radio emissions is proportional to the square of the exomoon's radius. Formation models show that exomoons can form around Jovian planets with masses up to 10^{-4} times the mass of their host planet (Canup & Ward, 2006). Therefore large exoplanets of $3 M_J$ or larger could form Mars-size exomoons, and $10 M_J$ exoplanets could have several Mars-size exomoons or larger (Heller & Pudritz, 2015). In contrast, smaller Jovians are unlikely to harbor large exomoons, unless those moons are captured, which

may be an uncommon occurrence; in the Solar System Triton of Neptune is the only large moon suspected to have been captured (Agnor & Hamilton, 2006). One big advantage of captured moons is that they appear to stay in retrograde orbits about half the time (Porter & Grundy, 2011), which have larger speeds relative to the local corotating plasma, and therefore produce more power than prograde moons for any given size.

Before an exomoon can exist, its host exoplanet has to exist, of course. In our observational proposals I try to target stars with confirmed exoplanets (e.g. Epsilon Eridani b), but since the intensity of the expected radio signals decays as the squared of the distance from Earth, I am forced to choose nearby star systems, most of which do not have confirmed exoplanets. Therefore, I use star metallicity as a criteria instead, since it is usually believed that stars with higher metallicity have a higher chance of forming planetary systems. In fact, stars with a metallicity similar to the sun ($[Fe/H] \geq -0.3$) are found to create exoplanets about 3% of the time, and the frequency of planet formation increases rapidly for $[Fe/H] > 0$, reaching more than 25% for $[Fe/H] > 0.3$ (Santos, et al., 2004). All the targets in my observational proposals have metallicity similar to the sun or larger. Additionally, formation models predict that even small stars can form Jovian exoplanets (Alibert, et al., 2011). However, planet formation does decrease with decreasing stellar mass, so I have to limit the observational searches to large M stars or larger. I also exclude white dwarfs due to the uncertainties in estimating the progenitor star's metallicity and mass. This restrictions on the existence of large exomoons may seem discouraging, but there are more than 50 M-type stars or larger within 15 light years of Earth, including two G stars (Alpha Centauri A and Tau Ceti), one F star (Procyon A), and one A star (Sirius A). Furthermore, among these stars there are more

than 10 suspected or confirmed exoplanets, including Epsilon Eridani b, which was a target on my successful proposal to GMRT.

This concludes the background sections of the dissertation. The following chapters will focus exclusively on the new research that was performed over the past two years as part of my dissertation project.

Chapter 4

Theory of Exomoon Radio Signals

The idea that exomoons can be discovered with radio telescopes (Noyola, et al., 2014) came from the observed interaction between Jupiter and its moon Io, which produces radio emissions in the tens of MHz (Hess, et al., 2008). The interaction between Io and the Jovian magnetosphere could also be found in exoplanet-moon pairs, and the resulting radio emissions could be used to directly detect these systems. Additionally, this detection technique has several advantages over other methods, including favoring exomoons orbiting *cold Jovians*, and that it works even if the system's orbital plane is not aligned with our line of sight. More importantly, radio detection constitutes a direct confirmation of both, the exomoon and its host planet, because the emission geometry of these systems (and thus their dynamic spectra) is unique.

This chapter will provide a summary of the sources of radio emissions found in the solar system, followed by an explanation of the mechanisms that allow Io to power the associated radio emissions. Then, there will be a detailed analysis of the characteristics of the exomoon signals, as well as the information that we can obtain from them.

4.1 Planetary Radio Emissions

There are many sources of radio signals in our Solar System and in the rest of the universe. In our solar system, radio signals come from several sources – man-made devices, the sun, lightning, auroral planetary emissions, and moon-induced planetary emissions – spanning a wavelength range from Hz to MHz. Figure 4.1 shows the frequency range and intensity of most planetary radio emissions in the solar system. There are several things to notice in Figure 4.1, including that most planetary radio emissions occur below Earth's ionospheric cutoff frequency (vertical dashed line), and

thus are not visible to ground radio telescopes. Only one of the emissions shown, the Io-DAM, is directly related to the presence of a moon (Io), and only that signal and Jupiter's non-Io-DAM have high enough frequencies to be observed from Earth. Finally, one can clearly see from the plot that Io-DAM radio emissions are at least one order of magnitude stronger than non-Io-DAM emissions for most of the applicable frequencies. Later it will be shown that these two emission types also have completely different dynamic spectra, and so one could easily differentiate one from the other. The fact that Io-DAM emissions are so intense and distinguishable from other types of emissions is what makes radio detection of exomoons feasible.

Non-satellite planetary radio emissions can be due to one of two sources: the

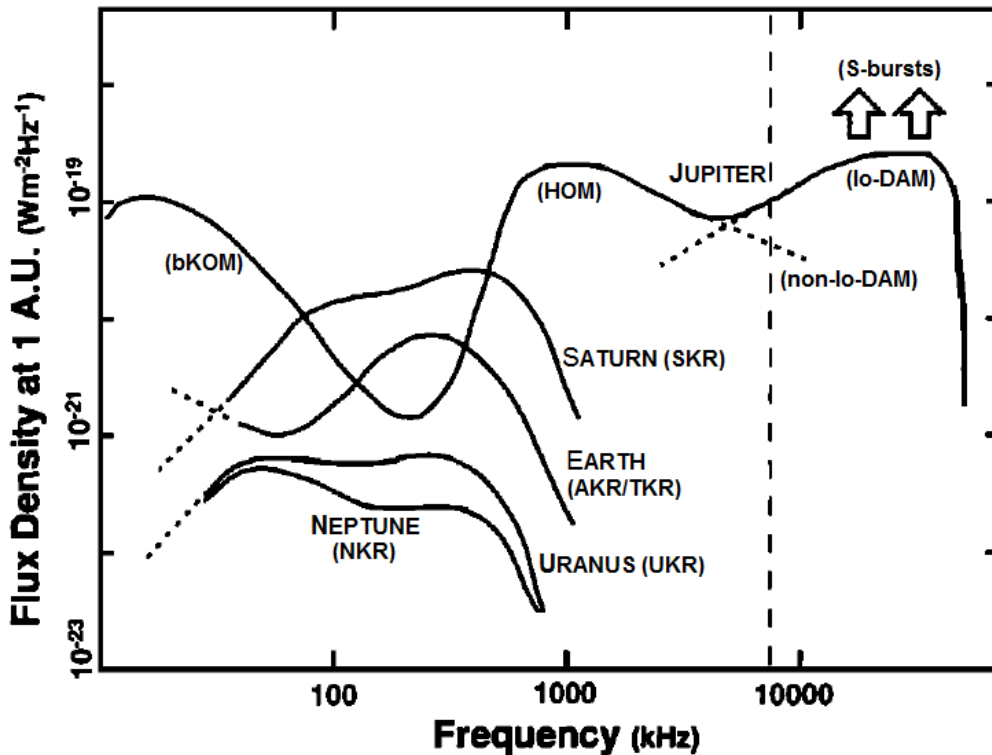


Figure 4.1. Summary of planetary radio emissions found in the Solar System. Taken from (Zarka, 1998)

solar wind (Zarka, et al., 2001), and magnetosphere-ionosphere coupling (Nichols, 2011).

4.2 Unipolar Induction Mechanism

It is widely known that a time-changing magnetic field induces currents in nearby conductors. This phenomena is described by Faraday's law of induction, which states that the electromotive force, \mathcal{E} , induced in a closed circuit is equal to the rate of change of the magnetic flux, Φ_B , enclosed by the circuit. Explicitly,

$$\mathcal{E} = -\frac{d\Phi_B}{dt}, \quad (4.1)$$

where the magnetic flux is defined by the integral

$$\Phi_B = \iint_S \mathbf{B}(\mathbf{r}, t) \cdot d\mathbf{S}, \quad (4.2)$$

or the amount of magnetic flux density, \mathbf{B} , passing through the surface S whose boundary is defined by the wire loop that makes the circuit. From Equations (4.1) and (4.2) one can see that to produce an electromotive force one has to have either a changing area or a changing magnetic field, the latter being the prevailing mechanism in electric motors and generators. In the absence of a varying \mathbf{B} or $d\mathbf{A}$, one can still generate an electric current through the effects of the *Lorentz* force. The Lorentz force states that the electromagnetic force acting on a point charge, q , due to an electric field, \mathbf{E} , and a magnetic field, \mathbf{B} , is given by

$$\mathbf{F} = q(\mathbf{E} + \mathbf{v} \times \mathbf{B}), \quad (4.3)$$

where \mathbf{v} is the velocity of the point charge relative to the magnetic field.

Now, if one places a conductor (free charges) in a uniform magnetic field, and then move the conductor at a steady pace (such that $\mathbf{v} \neq 0$ and there is no mechanical acceleration), we would see that a current is generated across the conductor, even

though \mathbf{B} remained constant. This happens because the left side of Equation (4.11) we purposely set to zero (the conductor is not accelerating, so the net force must be zero). Consequently, we can divide both sides by q , and solve for \mathbf{E} to get

$$\mathbf{E} = -\mathbf{v} \times \mathbf{B}. \quad (4.4)$$

If neither \mathbf{v} nor \mathbf{B} are zero, one can conclude that there is a nonzero electric field across the conductor. More importantly, this result is independent of the sign of the point charge, so negative charges do not cancel the effects of positive charges. This is the *Unipolar Inductor* effect (also known as the *Homopolar Inductor*). In circuits that obey Ohm's Law, the electric current density, \mathbf{J} , can be found from the electric field with the expression

$$\mathbf{J} = \sigma \mathbf{E}, \quad (4.5)$$

where σ is the conductivity of the conductor.

Combining Equations (4.4) and (4.5) it is found that

$$\mathbf{J} = -\sigma(\mathbf{v} \times \mathbf{B}). \quad (4.6)$$

Hence, if one wanted to know the current across the conductor one would just need to integrate Equation (4.6) over the shape of the conductor.

4.3 Moons as Unipolar Inductors: Electromotive Moons

Moons can interact with the magnetic fields and plasma in their environments to become electromotive moons, as is the case for Io. On Io, the volcanically produced plasma torus orbits Jupiter's magnetic equator at an angle of 9.6° from the rotational equator and co-rotates with the magnetic field at a speed of 74 km/s (Su, 2009). Io orbits Jupiter at a linear speed of 17 km/s, so Jupiter's magnetic field passes Io at a speed of 57 km/s. The speed difference gives rise to the unipolar induction (Goldreich & Lynden-

Bell, 1969), which induces a current across Io's atmosphere of a few million amps. The current then travels through the magnetic field lines to produce the characteristic radio emissions (Crary, 1997). It must be noted that while volcanism is essential to the formation of a dense ionosphere around Io, such a process might not be required for larger moons, since moons like Titan are already large enough to sustain a thick atmosphere, which in turn can give rise to an ionosphere. Furthermore, the unipolar inductor mechanism requires only a conductor, so any other conductive material, such as surface ice and water, can also act as the needed conductor. Hence, other moons like Europa, Ganymede, Titan, and Enceladus are known unipolar inductors, but their power is much lower than Io's, and so they do not produce any significant emissions other than

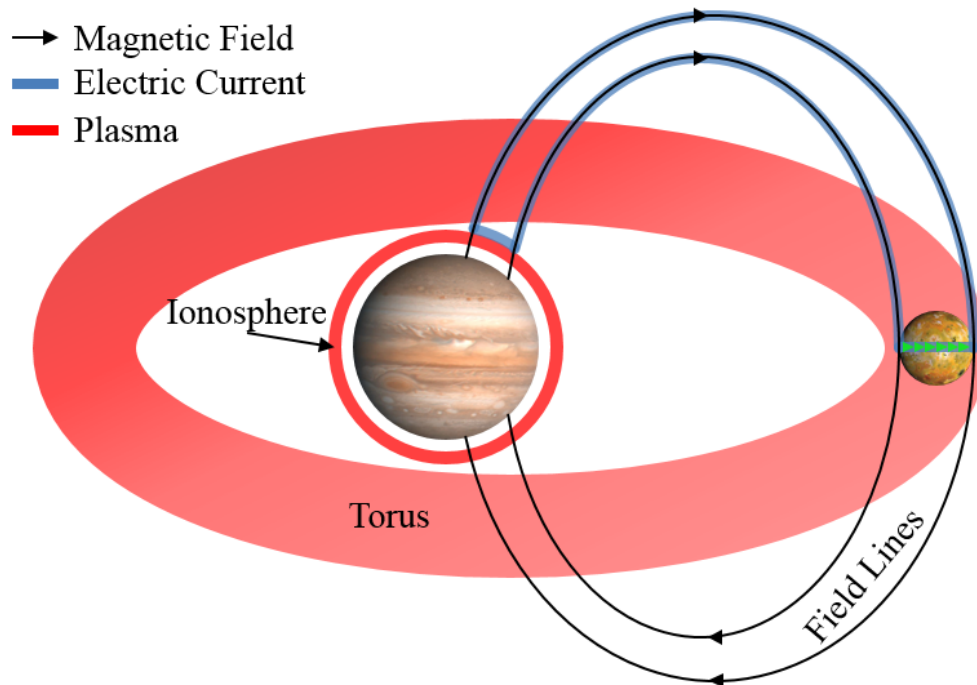


Figure 4.2. Jupiter-Io circuit diagram. The light green arrows over Io represent the current induced through the unipolar inductor mechanism.

visible and UV *auroral spots* at the poles of their host planets. Figure 4.2 shows a diagram of the circuit made by Io with Jupiter and the plasma torus.

4.4 Generation and Role of Alfvén Waves

Aside from an electric current, the interaction between Io and its plasma torus gives rise to *Alfvén waves* (Belcher, 1987). The precise mechanism by which these Alfvén waves interact with the torus is complex, and several analytical and numerical models have been proposed. In these models, Alfvén waves produce electric fields parallel to Jupiter's magnetic field lines, which then help transport electrons toward Jupiter's magnetic poles (Su, 2009) (Saur, et al., 1999) (Crary, 1997) (Neubauer, 1980). Alfvén waves are transverse waves which propagate along magnetic field lines. They do not change the magnitude of the local magnetic field, only its direction, and the component of the distorted magnetic field that is perpendicular to the original magnetic field is the one that produces the previously mentioned electric field through Faraday's law of induction. The same mechanisms that produce Alfvén waves can also produce *magnetosonic waves*, which are longitudinal waves that compress the magnetic field but do not change its direction. These magnetosonic can only produce electric field perpendicular to the original magnetic field, and therefore cannot transport electrons along the field lines. A diagram showing the difference between Alfvén and magnetosonic waves is shown in Figure 4.3.

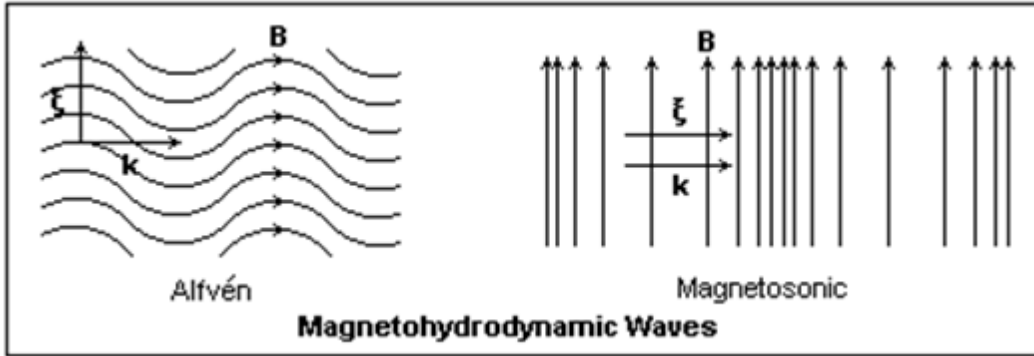


Figure 4.3. Alfvén waves vs Magnetosonic waves.

4.5 Signal Frequency, Bandwidth, and Periodicity

Radio emissions powered by satellites are produced by a process called the electron cyclotron maser instability, in which electrons in a magnetic field trap lose their energy in the form of electromagnetic radiation as they gyrate around the field lines. The frequency of these cyclotron emissions, the so called cyclotron frequency, is controlled by the strength of the magnetic field at emission site. Explicitly, the cyclotron frequency, f_c , is given by

$$f_c = \frac{e}{2\pi m_e} B, \quad (4.7)$$

where B is the magnetic field at the point of emission, e is the electron charge, and m_e is the electron mass. Writing the coefficient in Equation (4.7) explicitly yields the more convenient form $f_c = (2.8 \text{ MHz/Gauss})B$.

Since $R_s \ll r_s$, I take the field line that passes through the center of the exomoon to be the average field line. Given that each exomoon in the system is connected to a different field line, then to calculate the emission frequencies available to each exomoon I

need to know B at any point within that *specific* field line. Luckily, that problem is solved by Equation (2.10), which is restated below for clarity

$$B(r) = \frac{\mu_0 m_p}{4\pi r^3} \left(4 - 3 \frac{r}{r_s} \right)^{\frac{1}{2}}. \quad (4.8)$$

Within the path of the electrons traveling between an electromotive moon and the exoplanet, the largest magnetic field is found at the exoplanet's ionosphere (at $r \approx R_p$). Therefore, the maximum emitted cyclotron frequency is emitted at the exoplanet's ionosphere as well. Combining Equation (4.7) with Equation (4.8), and setting $r = R_p$ gives

$$f_{C,\max} = \frac{\mu_0}{8\pi^2} \frac{e}{m_e} \frac{m_p}{R_p^3} \left(4 - 3 \frac{R_p}{r_s} \right)^{\frac{1}{2}}. \quad (4.9)$$

Equation (4.9) is asymptotic, approaching a maximum value of $(\mu_0 e m_p)/(4\pi^2 m_e R_p^3)$ as r_s becomes very large. This value provides a maximum cut-off frequency for all the moons in the system. If the radius of the exoplanet is not known when calculating $f_{C,\max}$, many authors (e.g. see (Griessmeier, et al., 2007)) and references therein) choose to assume $R_p \approx R_j$. Studies on the radius-mass relationship of exoplanets show that $R_p = R_j$ is a good approximation for Jovian exoplanets (Mordasini, et al., 2012). Furthermore, many authors like (Zarka, et al., 2001) set $R_p = R_j$ unless the exoplanet's radius is explicitly known. Therefore I use this approximation $R_p = R_j$ also. For the case of Jupiter, with a magnetic dipole moment $m_j = 1.56 \times 10^{27}$ Am², and a radius $R_j = 69,911$ km, Equation (4.9) can be simplified to

$$f_{C,\max} = (12.8 \text{ MHz}) \left(4 - 3 \frac{R_J}{r_S} \right)^{\frac{1}{2}}. \quad (4.10)$$

So the maximum cyclotron frequency attainable around a planet like Jupiter is about 25.6 MHz. This asymptotic limit does not affect the detection of a single exomoon significantly, but as I shall show in section 4.8 (page 48) it will play an important role in how much information one can get from a multiple exomoon detection. Now that I can estimate the available cyclotron frequencies on the system, I can proceed to estimate just how strong these exomoon signals are.

4.6 Intensity of the Radio Emissions

In a previous section, I explained how Io, and other satellites, can become electromotive moons and power a celestial circuit. To find the total power dissipated by the circuit, Dr. Neubauer (Neubauer, 1980) assumed a simple current distribution around Io, and found that the maximum Joule dissipation of the system is given by

$$P_T = \pi R_{Io}^2 E^2 \Sigma_A, \quad (4.11)$$

where R_{Io} is Io's radius, E is the background electric field, and Σ_A is the conductance of the Alfvén wave current tubes. The electric field is simply $-V_\rho \times B_S$, where V_ρ is the plasma speed relative to Io, as found in Equation (4.4), and B_S is the strength of the magnetic field. In Neubauer's work, the conductance term is found to be

$$\Sigma_A = \frac{1}{\mu_0 \sqrt{V_A^2 + V_\rho^2}}, \quad (4.12)$$

where V_A is the Alfvén velocity, which in turn depends on the magnetic field, B_S , and the plasma density, ρ_S , as shown in Equation (4.13).

$$V_A = \frac{B_S}{\sqrt{\mu_0 \rho_S}}, \quad (4.13)$$

Since only a small fraction of the maximum Joule dissipation, P_T , is converted to radio waves, I will introduce the efficiency coefficient β_S , which previous studies have found it to be approximately 1% (Zarka, et al., 2001). There is little information on the variability of this parameter, so I assume that other exoplanet–moon systems have similar efficiency coefficients.

Hence, the maximum radio emission intensity, P_S , from these systems is given as

$$P_S = \frac{\pi \beta_S R_S^2 V_\rho^2 B_S^2}{\mu_0 \sqrt{B_S^2 / (\mu_0 \rho_S) + V_\rho^2}}, \quad (4.14)$$

where the subscript “Io” was switched to “S” to denote that these variables now belong to a generic exomoon or “satellite.” At this point in my research, I computed the plasma speed, V_ρ , assuming the plasma is in rigid corotation with the planet’s magnetic field, which is a good approximation to the Jupiter–Io case. Explicitly, if the moon orbits at a distance of r_S from the planet, then

$$V_\rho = \frac{2\pi r_S}{T_P} \mp \sqrt{\frac{GM_P}{r_S}}, \quad (4.15)$$

where G is the gravitational constant, M_P is the planet’s mass, and T_P is the planet’s rotation period. The ‘-’ and ‘+’ signs correspond to prograde and retrograde orbits, respectively. The other parameters in Equation (4.14) are explored in later sections.

Equation (4.14) does not depend on the properties of the host star and therefore the exoplanet–moon system does not have to be close to its star (or even have a host star) to be detectable. In fact, exomoons around exoplanets with small orbits might be

harder to detect because stellar winds can also induce radio emissions, which increase with decreasing planetary semi-major axis (Zarka, et al., 2001). Furthermore, moon-induced radio emissions do not solely occur along the orbital plane, which means the system's bodies do not have to orbit parallel to our line of sight.

The dependence of Equation (4.14) on R_s^2 clearly favors large exomoons. Although there has been no observational evidence, the possibility of detecting such exomoons is still plausible. Nevertheless, given that mass grows as the cube of the radius, the long-term stability of such systems can also be called into question (Musielak & Quarles, 2014); however, orbital stability analysis is beyond the scope of this study, so it will not be discussed any further.

Another expected size-related change is that if an exomoon is sufficiently large, it could also have its own magnetic field, but here I assume its effects to be negligible. However, based on the interaction between planets and the solar wind, I hypothesize that an exomoon's magnetic field would create a bow shock where the exomoon's magnetic field pressure equals the plasma torus pressure and its net effect should be to increase the apparent cross-sectional area of the exomoon, thereby increasing the power of the radio emissions. This effect will be discussed in more detail in later chapters.

4.7 Parameters and Assumptions

The intensity of exomoon-induced radio emissions depends on many parameters, thus a thorough clarification of how each of these parameters are treated is crucial. A very important parameter in the calculation of a radio signal's flux is T_p , but it is also very difficult to measure or predict. Therefore, it is typically assumed to be equal to Jupiter's rotational period, T_J , or that the planet is tidally locked if it is closer than 0.1 AU

to its host star (Lazio, et al., 2004). Since I mostly consider exoplanets with large orbits, I set $T_p = T_J$ throughout the calculations.

The atmospheric plasma density of an exomoon (or exoplanet) is difficult to determine if the environmental properties of the body are not already known. Even though the plasma density of an exomoon cannot be predicted, I found a reasonable estimate based on what is known about the solar system. The plasma density depends not only on the number of ions present, but also on the molecular weight of the ions that constitute it. For example, on Io, one can find O^+ , S^+ , SO^+ , etc., because Io's atmosphere is made from the SO_2 emitted by its volcanoes (Su 2009). Io's mean plasma density is $\approx 4.2 \times 10^4$ amu/cm³, or $\approx 7 \times 10^{-17}$ kg/m³ (Kivelson 2004). Earth's ion number density is typically on the order of 10^5 cm³, and the dominant ion is O^+ , which gives us a plasma density of $\approx 1.7 \times 10^6$ amu/cm³, or $\approx 2.7 \times 10^{-15}$ kg/m³ (Schunk & Nagy 2009). Venus and Mars also have similar plasma densities to Earth, with O^{+2} , and O^+ ions from CO_2 being the dominant species in their ionospheres (Schunk & Nagy 2009). Given the large variability of this parameter, I chose to work with three different values: 10^4 amu/cm³, 10^5 amu/cm³, and 10^6 amu/cm³, which cover most of the range of plasma densities that can lead to a detectable exomoon with reasonable size (as explained in the next section). The dependence of P_s on the plasma density, ρ_s , can be better appreciated by rearranging Equation (4.14) to get

$$P_s = \frac{\pi \beta_s R_s^2 B_s^2 V_\rho}{\mu_0} \sqrt{\frac{\rho_s}{\rho_s + \mu_0^{-1} (B_s/V_\rho)^2}}. \quad (4.16)$$

Equation (4.16) allows for the definition of a critical density

$$\rho_c = \frac{1}{\mu_0} \left(\frac{B_s}{V_\rho} \right)^2, \quad (4.17)$$

which in turn allows me to characterize the three limiting cases:

$$P_- \equiv P_S(\rho_S \ll \rho_C) = \pi\beta_S R_S^2 V_\rho^2 B_S \sqrt{\frac{\rho_S}{\mu_0}}, \quad (4.18)$$

$$P_C \equiv P_S(\rho_S = \rho_C) = \frac{1}{\sqrt{2}} \pi\mu_0^{-1} \beta_S R_S^2 B_S^2 V_\rho, \quad (4.19)$$

$$P_+ \equiv P_S(\rho_S \gg \rho_C) = \pi\mu_0^{-1} \beta_S R_S^2 B_S^2 V_\rho. \quad (4.20)$$

Evidently, P_S increases with increasing ρ_S , so systems with higher plasma densities are more likely to be observable. However, the rate of increase of P_S decreases until it becomes almost independent of the plasma density. In fact, whenever ρ_S reaches ρ_C , P_S is already at $\approx 71\%$ of the maximum possible power, P_+ . Nevertheless, the value of ρ_C could be relatively high, in which case this limiting effect would not be a matter of concern.

Regarding the orbital radius r_s , the only real physical constraint on the exomoon's orbit is that it must be close enough to the exoplanet to be well inside the magnetosphere and gravitationally stable, but farther than the Roche limit to avoid structural instability. However, I can also make use of Equation (4.16) to find orbits that might favor radio emissions, since exomoons in these orbits are the most likely to be detected. To do this, I plotted Equation (4.16) while varying only the orbital radius of the exomoon. The result, shown on Figure 4.4, shows that for prograde orbits P_S has a maximum in orbits larger than the synchronous orbit, so exomoons close to that maximum are more likely to be detectable. For retrograde exomoons, on the other hand, radio power monotonically increases with decreasing orbital radius, i.e. the closer they are to their planet, the larger the intensity of their signal. It is important to note that retrograde exomoons will always

have a larger power output than prograde exomoons under the same conditions, but at least in our solar system prograde moons far outnumber retrograde moons, so it is debatable whether the power advantage will really result in a larger number of detections.

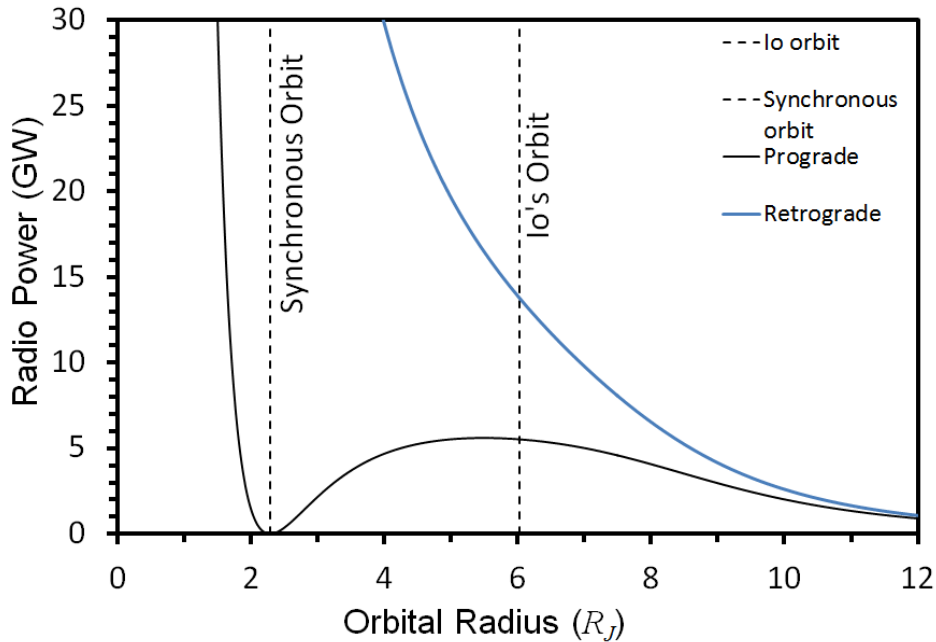


Figure 4.4. P_s plotted as a function of r_s , keeping all other parameters constant, for prograde and retrograde orbits. Io's orbit and the synchronous orbit are shown for reference.

Curiously, Io is in an orbit that allows it to radiate more 95% of the maximum. As lucky as this may sound, the prograde power function is fairly broad around the maximum, so much so that the region where an exomoon could radiate at least 95% of the possible maximum is about $2 R_J$, or one third the size of Io's orbit! (See Figure 4.5). Therefore, it seems reasonable to assume that an exomoon could be close to this maximum. In fact, the Saturnian moons Enceladus and Tethys also have orbits well within an area that would allow the moons to output at least 95% of the maximum

predicted radio power. Therefore, I will sometimes simplify calculations and comparisons of radio power by setting r_s to be the value that gives the maximum radio power. In such cases, r_s is renamed r_{Opt} to avoid confusion. It is noteworthy that the optimal orbital radius for each planetary mass needs to be found numerically, but it approximately follows a power law. For example, using $\rho_s = \rho_{Io}$ gives $r_{Opt} = 5.4 M_p^{0.32}$ where M_p and r_{Opt} are given in units of Jupiter's mass and radius. I also avoid the treatment of orbits smaller than the synchronous orbit due to their proximity to the Roche limit, as mentioned earlier.

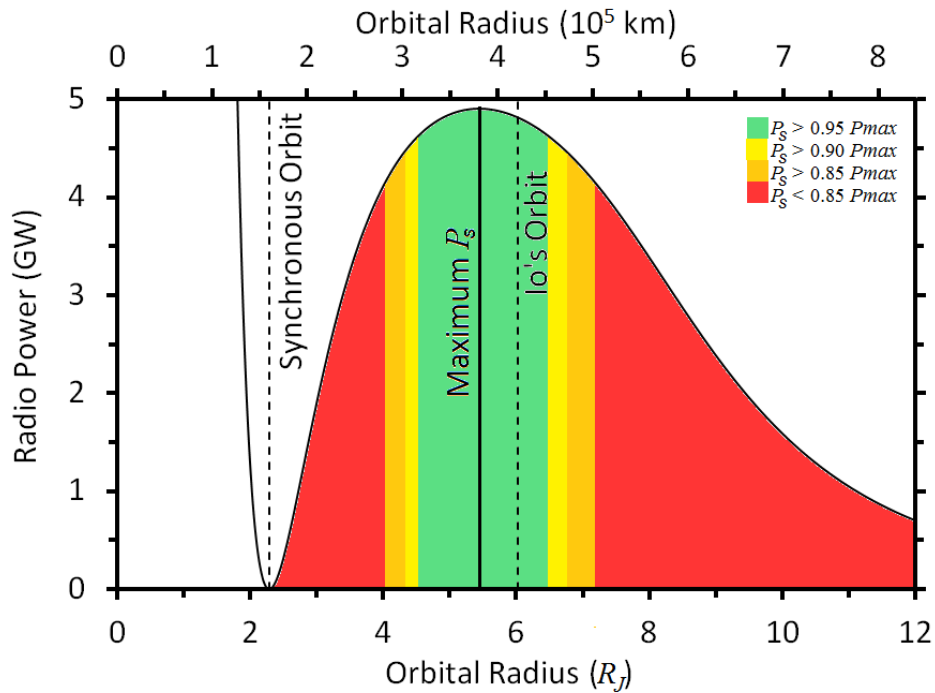


Figure 4.5. P_s plotted as a function of r_s for prograde orbits, and showing the radio power at each orbit compared to the maximum possible. Io's orbit and the synchronous orbit are shown for reference.

To analyze the effects of the other parameters on the power function $P_s(r_s)$, I plotted it in Figure 4.6 for a prograde orbits with various parameter combinations (results generalize to the retrograde case). The purpose of Figure 4.6 is to demonstrate how

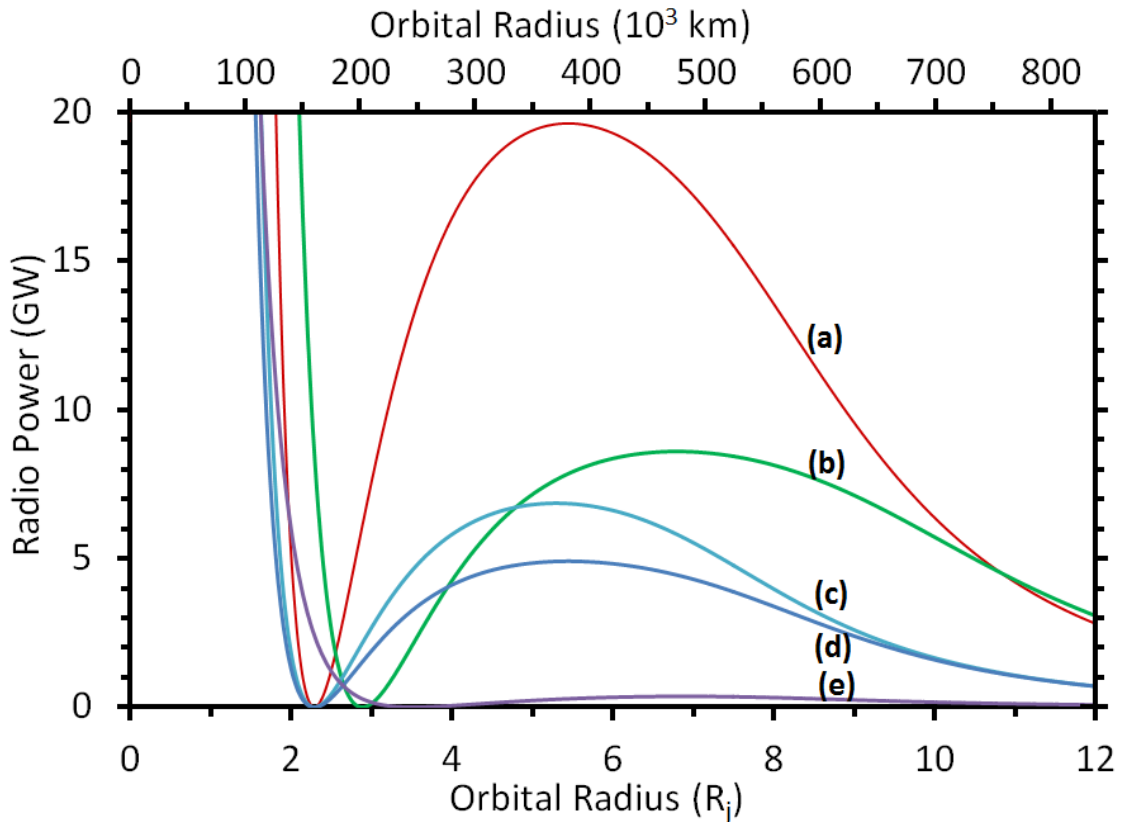


Figure 4.6. P_s plotted as a function of r_s , starting with values from the Jupiter–Io system and changing one parameter at a time. (a) $R_s = 2R_{Io}$, (b) $M_p = 2M_J$, (c) $\rho_s = 2\rho_{Io}$, (d) all Jupiter–Io values, (e) $T_p = 2 T_J$. The node seen at the synchronous orbit occurs because $V_\rho = 0$ at this orbital distance.

changing a single parameter in P_s affects its properties. The only parameter that does not affect the orbital distance at which this maximum occurs is R_s ; however, ρ_s only affects the point's position weakly and T_p is always held constant, so M_p is the dominant parameter when finding P_s 's maximum.

4.8 Detectability Limits

For a power source a distance d away from an observer, the incident signal flux is given by

$$S = \frac{P}{\Delta f \Omega d^2}, \quad (4.21)$$

where P is the source's output power, Δf is its bandwidth (taken to be half of the cyclotron frequency), and Ω is the solid angle through which the power is emitted by the source. In the case of the Io-DAM, the emission cone half angle ranges from 60° to 90° , with a wall thickness of 1.5° (Lopes & Spencer, 2007); (Queinnec & Zarka, 2001), which gives a solid angle of ≈ 0.14 – 0.16 sr. Assuming a system also emitting with a wide half angle and wall thickness of up to 2° gives $\Omega \approx 0.2$ sr. Taking P_S to be source's power, the incident flux becomes

$$S = \frac{2\pi\beta_S R_S^2 B_S^2 V_\rho}{\mu_0 f_C \Omega d^2} \sqrt{\frac{\rho_S}{\rho_S + \mu_0^{-1} (B_S/V_\rho)^2}}. \quad (4.22)$$

In (Noyola, et al., 2014) I calculated the maximum cyclotron frequency of the system using

$$f_C = \frac{eB_p}{2\pi m_e}, \quad (4.23)$$

which is just Equation (4.7) applied to the magnetic field strength at the poles of the exoplanet, B_p .

At the poles of the planet, the magnetic field is about twice as strong as it is at the equator. Hence, I can use Equation (2.15) to express the strength of the magnetic field at the poles as

$$B_p = 2 \left(\frac{r_S}{R_p} \right)^3 B_S, \quad (4.24)$$

where R_p is the radius of the exoplanet.

Combining Equations (4.22), (4.23) and (4.24) with the values for β_s and Ω , and simplifying yields

$$S = \left(\frac{\pi^2 m_e}{10\mu_0 e} \right) \left(\frac{R_s^2 B_s V_\rho}{d^2} \right) \left(\frac{R_p}{r_s} \right)^3 \sqrt{\frac{\rho_s}{\rho_s + \rho_c}}, \quad (4.25)$$

where the constants in the first parenthesis evaluate to $\approx 4.465 \times 10^{20}$ Jy·C/m, and the definition given on Equation (4.17) was used for aesthetic purposes. Equation (4.25) can now be used to solve for R_s to get

$$R_s = d \sqrt{\left(\frac{10\mu_0 e}{\pi^2 m_e} \right) \left(\frac{S}{B_s V_\rho} \right) \left(\frac{r_s}{R_p} \right)^3 \left(1 + \frac{\rho_c}{\rho_s} \right)^{\frac{1}{2}}}, \quad (4.26)$$

Now if S is taken to be the sensitivity of a radio telescope, then R_s becomes the required radius for an exomoon to be detectable by said radio telescope, given the other system parameters. Equation (4.26) is plotted on Figure 4.7 for the parameter values discussed in the text, and setting $r_s = r_{opt}$ for both prograde and retrograde cases, so that a direct comparison between the two can be made. The plasma density is kept at 10^5 amu/cm³, which is between the values for Io and Earth, and could reasonably be expected to coincide with large exomoons. The first noticeable aspect of Figure 4.7 is arguably the large difference between the prograde and retrograde cases, retrograde leading to detections about half the size of its prograde counterpart in all cases. More importantly, however, is the fact that the plot clearly shows that low frequency radio telescopes with sensitivities well in the tens of μ Jy are crucial in order to ensure a high chance of detection.

Additionally, it must be noted that the cyclotron frequency increases as $M_p^{1.15}$, thereby limiting the number of exoplanets that a telescope could successfully scan for

exomoons. Nonetheless, there is still a wide range of frequencies within which an exomoon with $R_S \leq 1 R_E$ could be detected up to 15 light years away, like cases where ρ_S is about 10^5 amu/cm^3 , and the telescope's sensitivity is at least tens of μJy (see Figure 4.7). The proposed SKA telescope, if fully implemented, could even detect Mars-size moons ($\approx 0.532 R_E$)⁴ if present.

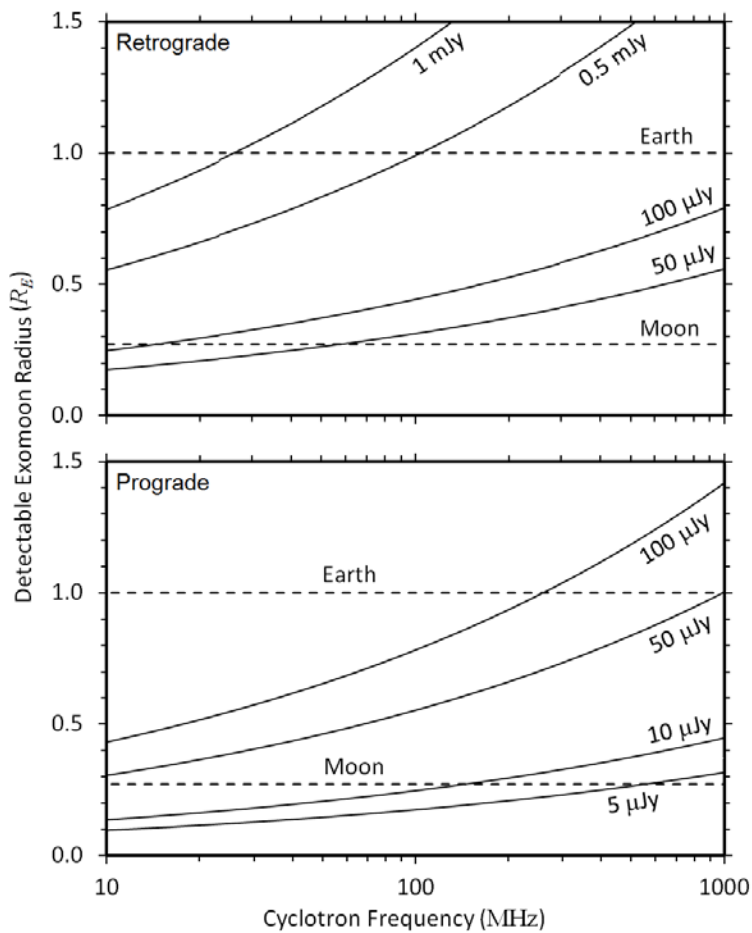


Figure 4.7. Radius of detectable exomoons in prograde and retrograde orbits for various flux sensitivities, for frequencies between 10 and 1000 MHz, and a plasma density of 10^5 amu/cm^3 . The distance to the system is set to 15 light years.

⁴ Assuming 2 polarizations, 1 hour of integration, and 16 MHz bandwidth

After the theoretical analysis, I applied the results to real systems. Specifically, the exoplanet Epsilon Eridani b ($1.55 M_J$, 10.5 light years away), we find that a telescope with a flux sensitivity of $S \leq 50 \mu\text{Jy}$ around 49 MHz could detect exomoons with radius between $0.24 R_E$ for high ρ_S ($\approx 10^6 \text{ amu/cm}^3$) and $0.73 R_E$ for low ρ_S ($\approx 10^4 \text{ amu/cm}^3$). For comparison, the Moon is $\approx 0.273 R_E$. On another nearby exoplanet, Gliese 876 b ($2.28 M_J$, 15.29 light years away), a telescope with similar sensitivity around 93 MHz could detect an exomoon with a radius between 0.28 and $0.86 R_E$, depending on ρ_S . In both cases, a fairly large minimum radius is required for exomoons to be detectable unless there is a large amount of plasma present. In fact, Equation (4.22) tells us that to find an exomoon of radius 2500 km (similar to Mercury or Titan) orbiting Epsilon Eridani b, we would need a telescope with a flux sensitivity of $14 \mu\text{Jy}$ if ρ_S is low. Nevertheless, improvements to radio telescope technology and observational techniques could one day make it possible to reach these sensitivities.

It must also be noted that in reality these systems emit over a range of frequencies instead a single one, so the range of detectable systems is effectively larger than shown here. It is also important to note that lower frequencies are important because planetary magnetic fields produce mostly decametric cyclotron emissions. Also, smaller exomoons can be detected at lower frequencies because they produce smaller emission bandwidth, thereby making the incident flux from Equation (4.22) higher. The calculation of the whole frequency band will be treated in future studies.

4.9 Possibility of False Positives

As mentioned previously, several types of planetary radio emissions exist within the solar system, but most are not related to the presence of satellites (auroral radio emissions). Among the different auroral radio emissions, the so called non-lo-DAM has

the property that it occurs on the same frequencies as the Io-DAM emissions. From this information, it would seem like non-Io-DAM emissions are the most likely to interfere with the detection of an exomoon. However, Io-DAM and non-Io-DAM emissions have completely different dynamic spectra. Explicitly, exomoon signals should show long, thin arcs lasting several hours, like those on the simulated Io-DAM dynamic spectra shown on Figure 4.8(a) (Taken from (Hess, et al., 2008)), whereas non-Io-DAM, and equivalent exoplanet signals, should show a wide-band, near-constant signals like those shown for a hypothetical hot Jupiter on Figure 4.8(b) (Taken from (Hess & Zarka, 2011)). Therefore, there is no risk of confusing one signal for the other.

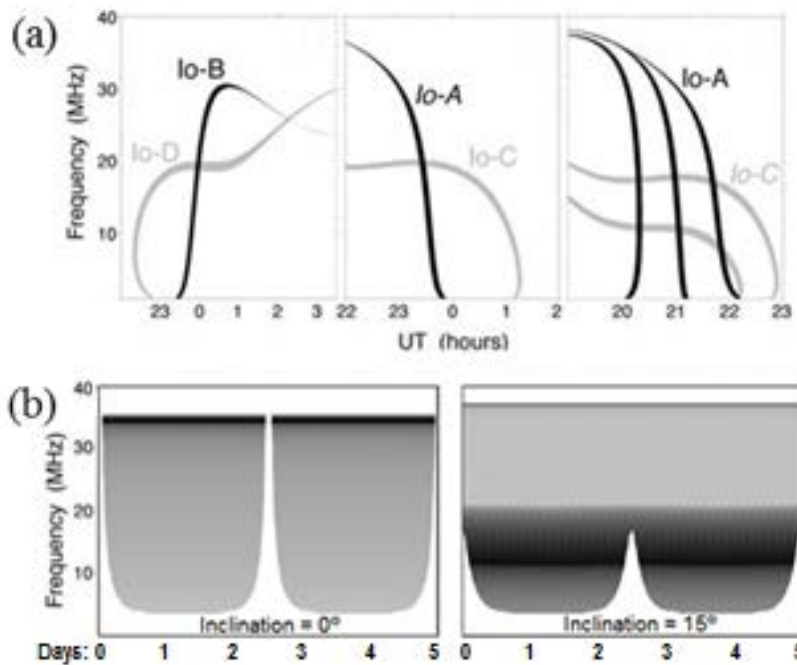


Figure 4.8. (a) Simulated dynamic spectra of typical Io-Jupiter arc emissions known as Io-A, Io-B, Io-C, and Io-D. The shade indicates the hemisphere from which the signal came, where black is for the Northern hemisphere and gray is for the Southern hemisphere [Taken from (Hess & Zarka, 2011)]. (b) Simulated dynamic spectra from an artificial Hot Jovian exoplanet with two orbital inclinations [Taken from (Hess & Zarka, 2011)]. Shade darkness represents relative intensity.

Chapter 5

Multiple-Moon Detections Through Plasma Torus Sharing

The focus of the previous chapter was on how one electromotive moon can be detected if it produces its own plasma. In this chapter, I will explore how two neighboring exomoons can share the same plasma, in such way that it allows both exomoons to power radio emissions of detectable amplitude.

5.1 Plasma Torus Topology

This sharing of plasma is possible because the rotation of the planetary magnetic field can drive the co-rotating plasma radially outwards. The main physical reason for this outwards movement is due to orbital mechanics: if there is an object in a circular orbit, and then an angular acceleration is applied to the object, it results in a radial acceleration either outwards or inwards, depending on the direction of the angular acceleration. In our case, the plasma starts from Io's orbit (which is nearly circular) and is accelerated to the co-rotation speed, obtaining an outwards radial velocity in the process. Furthermore, the co-rotation speed is larger than the local orbital speed for all orbits larger than the synchronous orbit. For Jupiter, the synchronous orbit is located at $\approx 2.29R_J$, which is smaller than Io's orbital radius, so the Jovian magnetic field continuously accelerates Io's plasma outwards, giving the plasma torus its current shape. Figure 5.1 shows the Io plasma torus density distribution, replotted from (Bagenal, 1994). The data from Figure 5.1 was fitted using a natural cubic spline algorithm; high precision was kept to ensure numerical agreement with the original data.

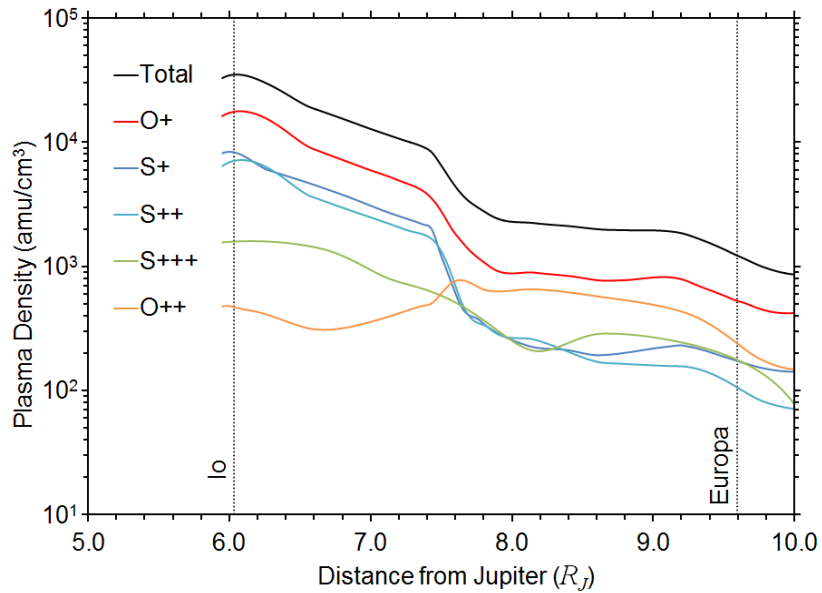


Figure 5.1. Io's plasma torus density profile shown as a function of distance from Jupiter between 6 and 10 R_J [Adapted from (Bagenal, 1994)]. The orbits of Io and Europa are shown for reference. Note: $1 \text{ amu/cm}^3 = 1.66 \times 10^{-21} \text{ kg/m}^3$, and $1 R_J = 69,911 \text{ km}$.

It can be seen from the figure that Io's plasma torus extend a significant distance behind Io, and it is especially dense for distances below $7.5 R_J$. The sharp decrease in plasma density seen between 7.5 and $8 R_J$, known as the ramp, is believed to be caused by Jupiter's ring current (Siscoe, et al., 1981). The ionic composition and detailed features of extra-solar plasma tori may vary for each system, but the characteristics that give rise to the general shape of the plasma distribution are quite general. These characteristics include: (i) a central mass to orbit, like Jupiter; (ii) a source of plasma strong enough to sustain a torus, like Io; (iii) a satellite to interact with the plasma, also like Io; and (iv) a rotating magnetic field, like on Jupiter. All these properties are required to obtain a co-rotating, radially-expanding plasma torus whose behavior should be similar to that of Io's. I will now use this plasma torus to demonstrate that sharing plasma can effectively lead to detection of multiple exomoons.

5.2 Corotation Plasma Velocity

Before I can continue with this analysis, a refinement needs to be made to the plasma velocity. In the previous chapter it was assumed that the plasma in the torus had exactly the same angular velocity as the Jovian magnetic field, i.e. that it was in rigid-corotation. That approximation was fine because the model described a single exomoon interacting with its own plasma. Conversely, now there is a comparison between the effects of two different exomoons, and so deviations from rigid corotation might become important. As before, the relative plasma velocity, V_p , has two components: the exomoon's orbital velocity, and the corotation velocity. Assuming the exomoon is in a near circular orbit of radius r_s , so its orbital velocity, V_{orb} , is given by,

$$V_{orb} = \sqrt{\frac{GM_p}{r_s}}. \quad (5.1)$$

To calculate the corotation velocity, V_{co} , I use the fit to Jupiter's observational data

$$V_{co} = v_0 \left(1.12 - \frac{r_s}{50R_J} \right) \left(\frac{r_s}{R_J} \right), \quad (5.2)$$

found by (Bagenal & Delamere, 2011), where $v_0 = 12.6$ km/s, and which is valid for distances up to $\approx 28R_J$. The plasma corotates with the planetary magnetic field in near-rigid corotation (which in turn rotates with exoplanet), so the plasma's rotation is always prograde, unlike the exomoon which can be either prograde or retrograde. Exomoon plasma tori have not been well studied. To the best of our knowledge, as of the time of this study (Johnson & Huggins, 2006) and (Ben-Jaffel & Ballester, 2014) are the only articles fully dedicated to exomoon plasma tori. Hence, a generalization of Equation (5.2) will not be attempted at this time.

Combining Equations (5.1) and (5.2), V_ρ is found to be given by

$$V_\rho = v_0 \left(1.12 - \frac{r_s}{50R_J} \right) \left(\frac{r_s}{R_J} \right) \mp \sqrt{\frac{GM_P}{r_s}}, \quad (5.3)$$

where the '-' and '+' signs correspond to prograde and retrograde exomoon orbits, respectively. The direction of rotation of the exomoon makes a big difference. As shown in Equation (5.3) and Figure 5.2, retrograde exomoons will have larger V_ρ than prograde exomoons. Since P_s is proportional to V_ρ , then one can conclude that retrograde exomoons will generate more radio power, and thus have a better chance to be detected. Additionally, $V_\rho = 0$ when prograde exomoons are near the synchronous orbit (see Figure 5.2), so $P_s = 0$ as well, making detections on these orbits impossible. The retrograde case does not have this problem, although V_ρ does have a minimum value close to the

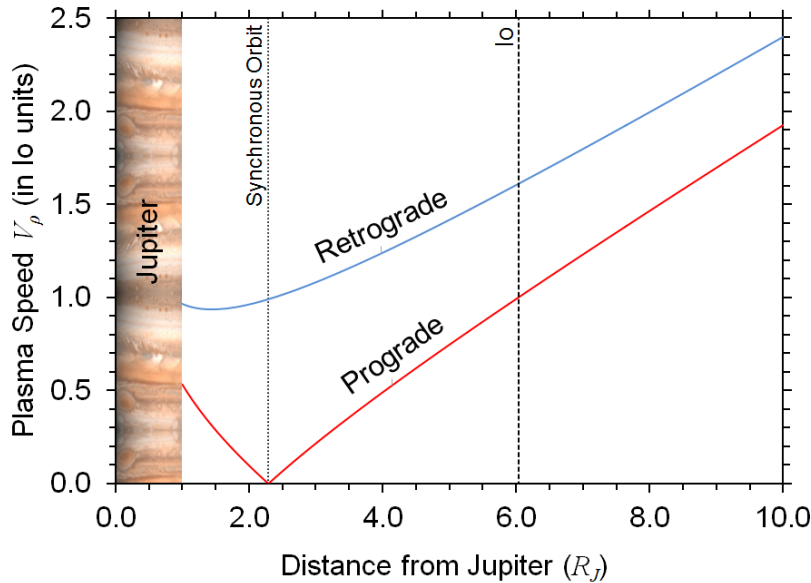


Figure 5.2. Relative speed between the corotating plasma and a Jovian moon, V_ρ , for orbits between 1 and 10 R_J , expressed in Io units (1 unit ≈ 56.8 km/s). Io's orbit and Jupiter's boundary are shown for reference.

planet's surface, as can be seen from the figure.

Now that I have a well-defined plasma speed function, I can proceed to illustrate the plasma torus sharing mechanism. To do so I will substitute Jupiter's moon Europa for a hypothetical exomoon. I will change the exomoon's radius, and orbital distance to simulate the scenarios that could be encountered in exoplanetary systems. For R_s we will use the three values corresponding to Io (1821.3 km), Europa (1560.8 km), and Ganymede (2631 km). As for the orbital radius, r_s , the exomoon has to remain orbitally stable, so it cannot be too close to Io ($r_s \approx 6.03 R_J$), neither can it be too far away that the plasma torus is too diluted to cause any significant effect either. For the latter, we chose to use the upper limit $r_s \leq 10 R_J$. For the lower limit, it seemed sufficient for our purposes to simply keep the satellites outside each other's Hill spheres. The radius of the Hill sphere, R_H , is given by

$$R_H \approx a(1 - e) \left(\frac{M_s}{3M_p} \right)^{\frac{1}{3}}, \quad (5.4)$$

where a , e , and M_s are the semi-major axis, eccentricity, and mass of the moon, respectively. When Equation (5.4) is applied to Io, Europa, and Ganymede the largest Hill radius found is that of Ganymede at $0.453 R_J$. In other words, we can choose our exomoon's smallest orbit to be $6.5 R_J$, and still have all satellites be outside each other's Hill sphere. Thus, our range of study is $6.5 R_J \leq r_s \leq 10 R_J$. I excluded Callisto because its orbit ($a \approx 26.9 R_J$) is too far away from Io to be relevant for this study. For clarification, this study does not intend be a complete exomoon orbital stability analysis, but only to provide a range of orbital distances where the exomoon can reasonably be expected to

survive in the long term. A more thorough discussion of exomoon orbital stability can be found in studies such as (Musielak & Quarles, 2014).

5.3 Signal Power and Flux density

Now that all necessary parameters are defined, I can proceed to calculate the power and flux density of the radio signals for the previously mentioned values of R_s and r_s , for the prograde and retrograde cases. Applying Equation (4.16) first to Io (prograde) results in a radio power of ≈ 4.9 GW; this value will be used for comparisons later on. Next, applying Equation (4.16) now to the rest of the cases yields the results shown in Figure 5.3. The results from the figure show that plasma torus sharing can be an extremely important mechanism for making electromotive moons detectable. For

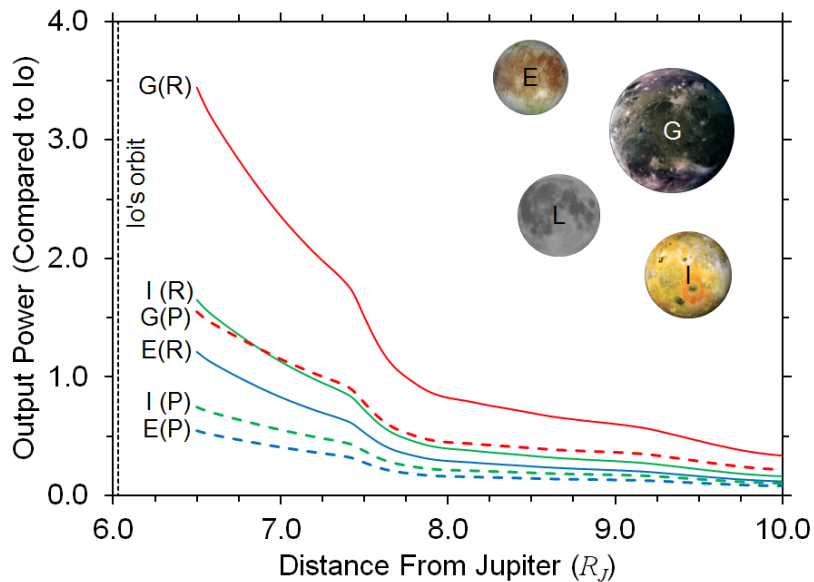


Figure 5.3. Radio emission output power, P_s , calculated for various exomoon sizes in orbits between 6.5 and 10 R_J . The labels (P) and (R) denote prograde and retrograde configurations. We used the sizes of the Galilean satellites Europa, Io, and Ganymede as examples (labels E, I, and G respectively). All the moons used, as well as Earth's moon, L, are shown to scale for comparison. Power is given in Io units, where 1 unit ≈ 4.9 GW, as calculated by the model.

example, if I_o is detectable then either a Ganymede-size prograde exomoon, or an I_o -size retrograde exomoon would also be detectable up to $r_s \approx 7.3 R_J$ away from Jupiter. More strikingly, a Ganymede-size retrograde exomoon would be twice as powerful as I_o at this distance, and be detectable up to $0.5 R_J$ farther than the exomoons in the previous example. In other words, this Ganymede-size retrograde exomoon could be detectable even if the plasma source is not. The latter case attests to how prominent the effects of plasma torus sharing can be. It is important to notice that the ring current near $r_s \approx 7.5 R_J$ is a strong plasma sink, and it significantly limits plasma sharing beyond its location, which is why exomoons in this example need to be at most $1.5 R_J$ apart for a successful double detection. If ring currents are common around other Jovian exoplanets then they would limit plasma sharing there too, unless those currents occur beyond the orbit of at least two electromotive moons, then they would not be a problem.

To obtain the emission's flux density, we need to recall Equation (4.21), which is given again as Equation (5.5) for convenience.

$$S = \frac{P}{\Delta f \Omega d^2}, \quad (5.5)$$

Using the approximation $\Omega \approx 0.16$ steradians, and taking advantage of the results from Figure 5.3, I can write the flux density as

$$S = (2.7 \text{ mJy}) \left(\frac{P_s}{P_{I_o}} \right) \left(\frac{24 \text{ MHz}}{f_{C,\max}} \right) \left(\frac{1 \text{ ly}}{d} \right)^2, \quad (5.6)$$

where the ratio P_s/P_{I_o} can be obtained from Figure 5.3, and $f_{C,\max}$ can be calculated from Equation (4.10).

5.4 Physical Properties Derived from Multiple Detections

Let T_s be the orbital period of an exomoon, then Newton's laws state that the relationship between r_s and T_s is given by

$$r_s^3 = \frac{GM_p}{4\pi^2} T_s^2. \quad (5.7)$$

Dividing Equation (5.7) by $(4/3)\pi R_p^3$, I find that the density of exoplanet, D_p , can be expressed as

$$D_p = \frac{3\pi}{GT_s^2} \left(\frac{r_s}{R_p} \right)^3, \quad (5.8)$$

but the ratio r_s/R_p needs to be known in advance. If the signals of at least two exomoons are detected in a system, that information can be used to calculate the ratio. Knowing the maximum frequency and orbital period for two exomoons, (T_i, f_i) and (T_j, f_j) , and using Equation (4.9) yields

$$\left(\frac{f_i}{f_j} \right)^2 = \left(\frac{r_j}{r_i} \right) \frac{4r_i - 3R_p}{4r_j - 3R_p}, \quad (5.9)$$

which can be further rearranged to obtain

$$\frac{r_i}{R_p} = \frac{3}{4} \left(\frac{f_j^2 - (r_i/r_j)f_i^2}{f_j^2 - f_i^2} \right). \quad (5.10)$$

Notice the ratio r_i/r_j is still needed; however, this ratio can be easily obtained because both exomoons orbit the same exoplanet. Using Equation (5.7) with r_i and r_j , we quickly find that

$$\frac{r_i}{r_j} = \left(\frac{T_i}{T_j} \right)^{\frac{2}{3}}, \quad (5.11)$$

which gives the last piece of data needed to calculate the D_p . Also, Equation (5.10) can be solved for either exomoon, and each solution can be used to calculate D_p separately. Hence, the values of D_p can be averaged to further reduce the uncertainty by a factor of $\sqrt{2}$. Even better, now that r_s/R_p and D_p are known, and if R_p is also known (e.g. from planetary transits), then r_s , M_p and m_p can also be calculated. In other words, a multiple-exomoon detection allows us to readily calculate almost all the system's physical quantities without the need for complex numerical methods.

5.5 More Plasma Sources

The previous discussion was focused on one exomoon (the receptor) using plasma from a neighboring exomoon (the donor) to become detectable. However, the receptor exomoon itself can also be a source of plasma. For example, (Bagenal, 1994) noted that the increase in oxygen ions seen past $7.5 R_j$ in Figure 5.1 could mean that Europa is also a source of plasma for the system. Later studies corroborate this statement, and further state that Europa can sustain an average plasma density of ≈ 2500 amu/cm³, which is much less than Io (≈ 42300 amu/cm³), but significantly larger than Ganymede (≈ 54 amu/cm³), and Callisto (≈ 1.6 amu/cm³) (Kivelson, 2004). To illustrate, the exomoon c on Figure 5.4 receives plasma from exomoon b but it also produces its own plasma torus, and uses the combination of both plasmas to generate currents. In contrast, exomoon d does not produce its own plasma torus, but it can still use the plasma provided by exomoons b and c . Similarly, the exoplanet itself could be the source of plasma for an exomoon that cannot produce its own. An exomoon of this type, which

depends solely on the plasma trapped in the exoplanet's magnetosphere to produce currents, is illustrated by exomoon a on Figure 5.4.

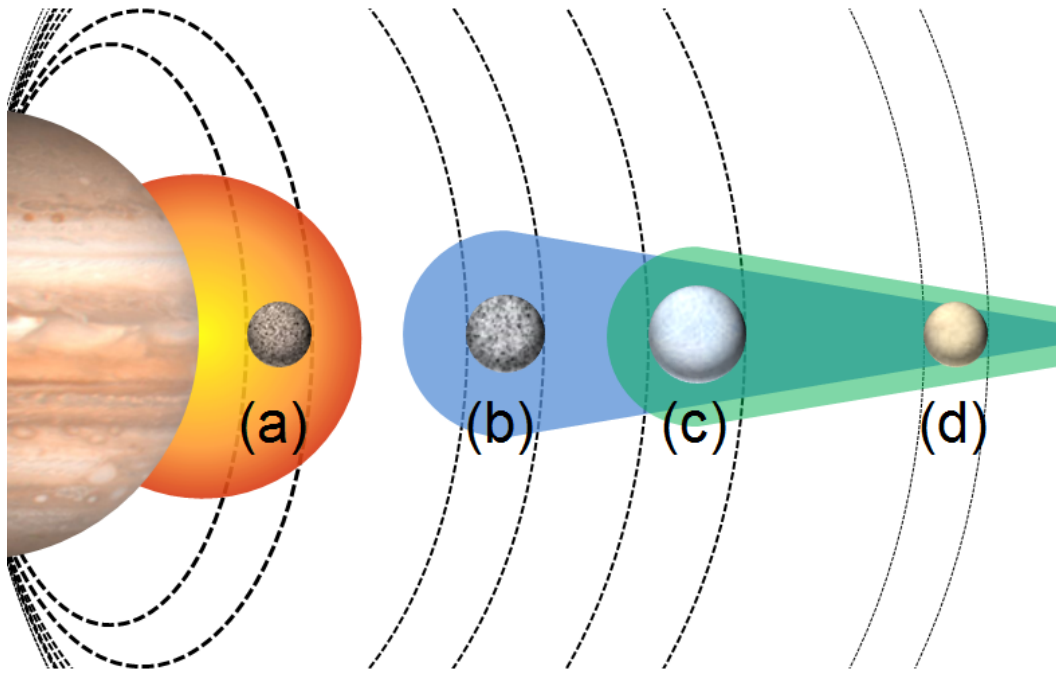


Figure 5.4. Four pathways through which an exomoon could become a detectable electromotive moon: (a) An exomoon using a hot Jupiter's magnetospheric plasma; (b) An exomoon which, like Io, provides enough plasma to create a dense torus; (c) An exomoon whose plasma torus is a combination of its own ionospheric plasma, and the plasma from a donor exomoon; and (d) An exomoon which relies solely on the plasma from one or more donor exomoons. The dashed curves are the field lines which connect the exomoons to the exoplanet's magnetic poles. Image Credit: Jupiter Photo NASA/JPL/Caltech (NASA photo # PIA00343)

Chapter 6

Exomoon Radio Detection

6.1 Previous Detection Attempts

Before radio detection of exomoons was suggested in Noyola et al (2014), various groups were already searching for exomoons using other techniques. Most notably, David Kipping started the Hunt for Exomoons with Kepler (HEK) project, which intended to find exomoons using transit data (Kipping, et al., 2013).

6.2 Prospective Observational Facilities

Based on the parameters and limits established in Chapters 4 and 5, I now proceed to assess the model's testability with currently available, or soon to be available, radio telescopes. Of all the telescopes I looked at, there were four whose capabilities were most likely to be able to detect electromotive moons. The four radio telescopes were LWA (Kassim, et al., 2005), LOFAR (van Haarlem, et al., 2013), GMRT (<http://gmrt.ncra.tifr.res.in/>), and SKA (<http://www.skatelescope.org/>).

To evaluate the suitability of the telescopes, I will begin by plotting their respective flux sensitivities for each frequency in their range. When calculating each telescope's expected sensitivity, I assume 2 polarizations, 1 hour of integration, and a 16 MHz bandwidth, or best known sensitivity if available data is not enough to make a more accurate calculation. The resulting plots are given in Figure 6.1.

Next, I will use the previous results to find the minimum radius of the exomoons that these telescopes could theoretically detect for various scenarios. Also, I use the relationship between cyclotron frequency and exoplanet mass ($f \propto B \propto M^{1.15}$) to use the latter parameter as the abscissa instead of frequency.

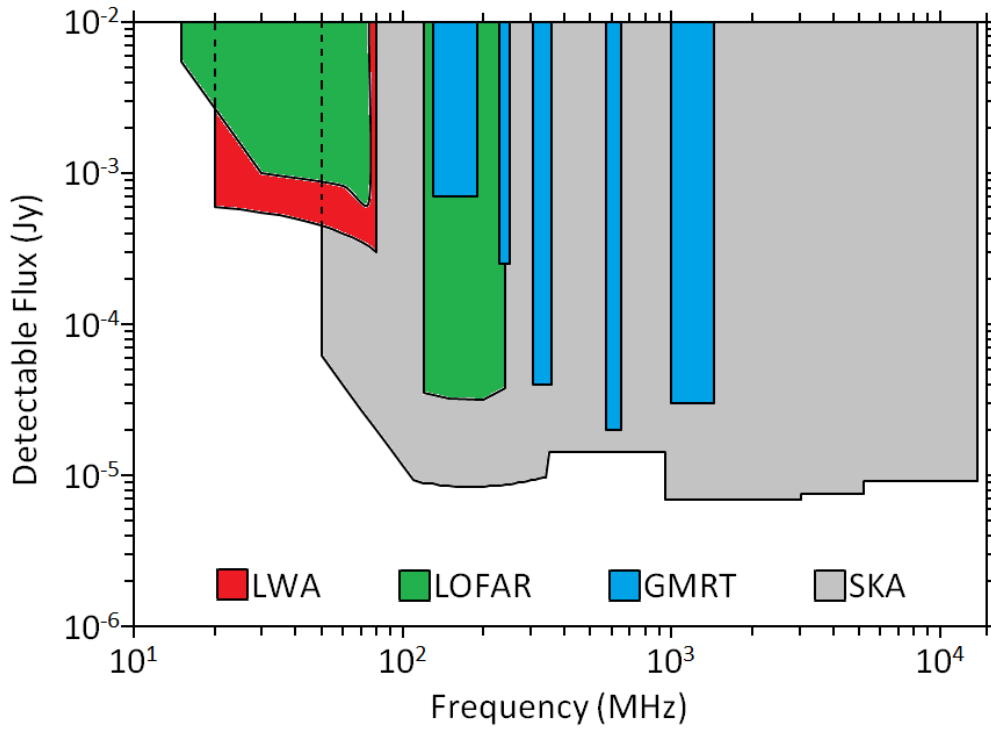


Figure 6.1. Flux sensitivities (in Janskies) vs frequency for each of the four telescopes evaluated.

6.2.1 LWA and LOFAR

Two of best decameter radio telescopes available to search for exomoons are LWA and LOFAR. LWA operates in the frequency in the 20-80 MHz range, and it is located near Santa Fe, New Mexico. LOFAR, located in northern Europe, has two antennas: a low band antenna (LBA) operating between 15-75 MHz, and a high band antenna operating between 120-240 MHz. The sensitivity information for these two telescopes had to be extrapolated from limited published data points. For the LWA sensitivity calculations, I used the following linear extrapolation

$$S_{LWA} = -0.0035(f - 30) + 0.39, \quad (6.1)$$

where S_{LWA} is the telescope's flux sensitivity in mJy (1 Jansky = $1e-26$ W/m²Hz), and f is the observation frequency in MHz. Similarly, LOFAR's HBA capabilities are modeled with the cubic polynomial

$$S_{LR} = 10^{-4} [7 \times 10^{-5} f^3 - 0.03 f^2 + 3f + 157]. \quad (6.2)$$

LOFAR's LBA needed to be extrapolated by three different functions, which made it too inconvenient to show here, but each resulting curve was almost linear. The results from these calculations are shown in Figure 6.2. From the plot, it can be seen that LOFAR's HBA can detect the smallest exomoons, but the host planet has to be 3-4 Jupiter masses to emit in high enough frequencies to be seen by the antenna. The second best choice LWA, which could detect down to Earth-size exomoons, but it would require a lot more plasma in the exomoon's environment, and either a 1-2 Jupiter mass exoplanet, or a more massive exoplanet but which is much less magnetic than the predicted with the present model.

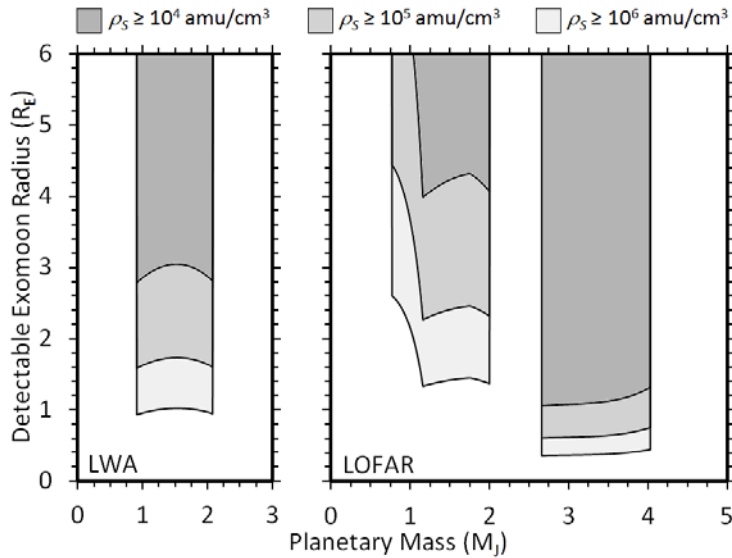


Figure 6.2. Radii of exomoons potentially detectable with LWA and LOFAR.

When attempting to search for exomoons with a radio telescope, there is yet another requirement that must be fulfilled in addition to sensitivity and frequency range: telescopes can only see a certain range of latitudes in the night sky (called the *declination* limits), so the target systems must be within those limits. To illustrate, Figure 6.3 shows nearby star systems that might be used as targets for a search with LOFAR. LOFAR can only see targets with declination above 0° , shown as a thick horizontal line on the figure, so everything below this line cannot be observed by LOFAR. Additionally, LOFAR can see multiple targets at the same time if they are all within 20 arcseconds of each other. Hence, the circles shown in Figure 6.3 are made to be 20 arcseconds wide, so the targets that overlap can be observed simultaneously and are therefore preferable.

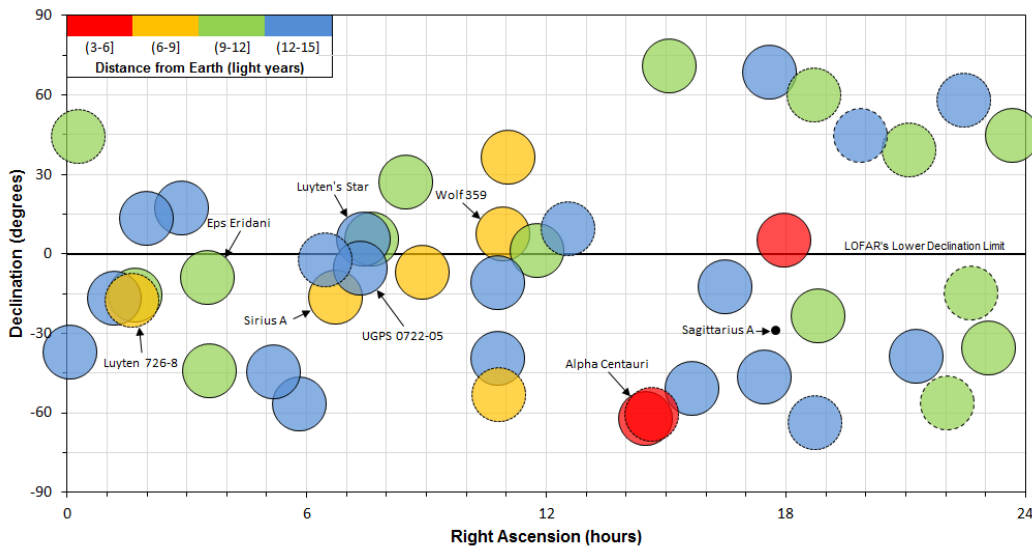


Figure 6.3. Position of all nearby stars within 15 light years from Earth, plotted in spherical coordinates. The size of the circle has a diameter of $20''$, the color tells the star's distance from Earth, and the circle's outline tells how many stars are in the system (solid for singles, fine-dotted for binaries, and coarse-dotted for triples).

6.2.2 GMRT

GMRT is located in northwestern India, and has several frequency bands available, as can be seen in Figure 6.1. It has good sensitivity although the exoplanet

mass needed to reach the available frequencies is a little big. However, GMRT does have the advantage of having very large declination limits, from -54° to $+90^\circ$, or 80% of the night sky.

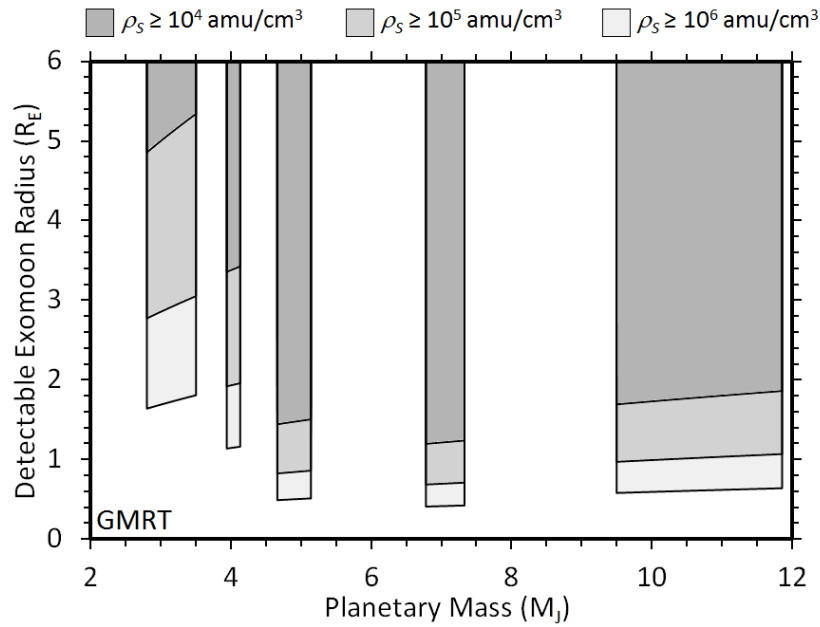


Figure 6.4. Radii of exomoons potentially detectable with GMRT.

My collaborators and I applied for observation time at GMRT, and were granted 9 hours of observation for 3 targets. All our targets, and their location in the sky are shown in Figure 6.5.

The analysis of the GMRT data is still ongoing, but the preliminary results, shown in Figure 6.6, indicate that there are no sources stronger than 0.5 mJy in the Epsilon Eridani system 325MHz and 1400MHz. The target system is at the center of the green circle on the image.

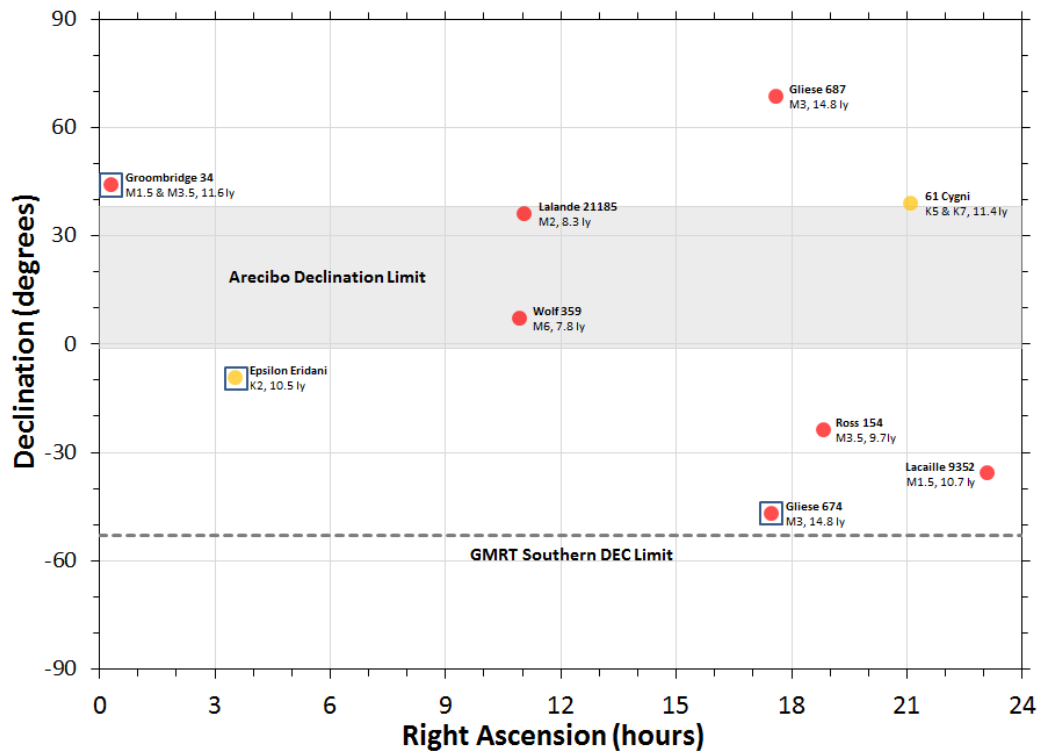


Figure 6.5. Targets proposed to GMRT. Targets inside the blue squares are observed targets. The Arecibo declination limit is shown as a comparison to the GMRT declination limit.

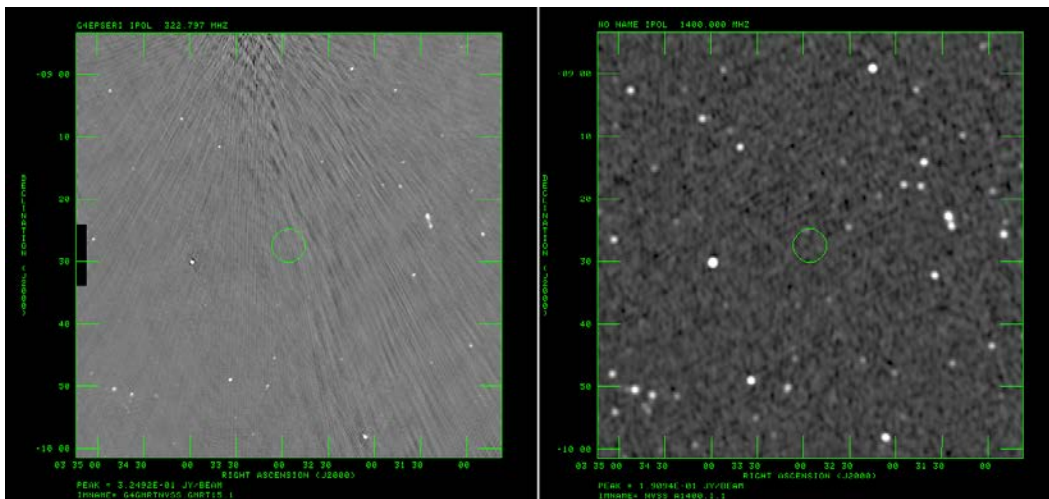


Figure 6.6. Preliminary results from the GMRT target Epsilon Eridani.

6.2.3 SKA

Currently under construction, SKA, or the Square Kilometre Telescope, will be the largest telescope on Earth when finished, and will have stations across Australia, New Zealand, and South Africa. It will observe from 50MHz to several GHz, but only the lowest frequencies are relevant to my research.

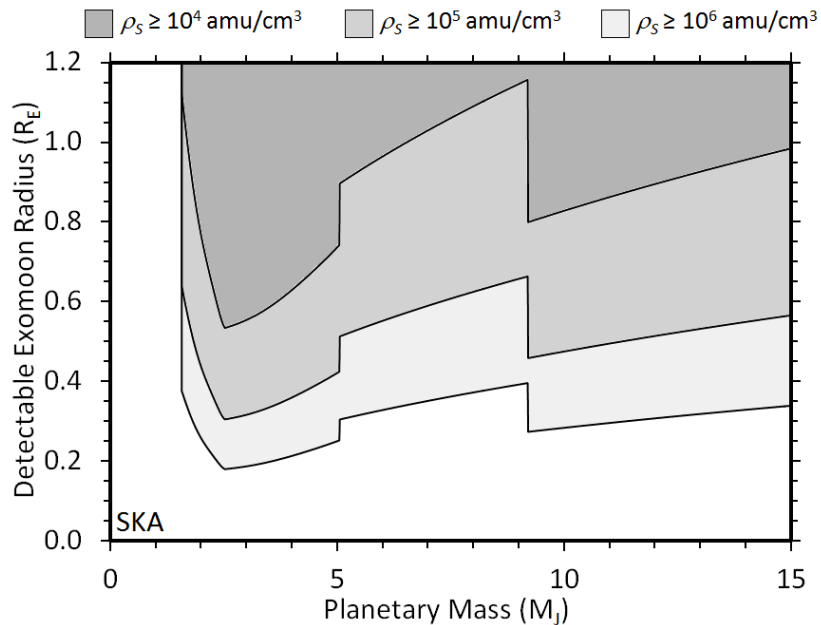


Figure 6.7. Radii of exomoons potentially detectable with SKA.

From Figure 6.7 it is clear that SKA will be one powerful tool for searching for exomoons. Additionally, the above quantities were calculated using a 16MHz bandwidth, but it is not uncommon to have 32MHz bandwidths available as well, which would decrease the required size of detectable exomoons by a factor of $\sqrt{2}$.

6.2.4 Other Facilities

Aside from these four telescopes, my collaborators and I were invited to collaborate with Arecibo scientists, so we will pursue getting time on that telescope also. Moreover, a recent private sponsor made it possible to build the new Owens Valley LWA

(OV-LWA), which is an all sky survey at 28 - 88MHz, to be commissioned next year, and whose data might become public access, thereby removing limitations on observational time and target quantity. Nevertheless, these news have not been confirmed yet, but I will keep in touch with the people involved, and follow their progress.

Chapter 7

Prospective Research Plans

First and foremost, the analysis of the observational data from GMRT is a priority. Per current estimates, cleaning and calibrating should be finished by the end of May, 2016. Then the final results must be published in an appropriate journal. I will be applying again for time at GMRT in January, and will also apply to Arecibo in March, and apply to LOFAR jointly with the Polish consortium of LOFAR scientists.

The theoretical part of the exomoon radio detection model needs enhancements to cope with more realistic scenarios. The possibility of exomoons with intrinsic magnetic fields could potentially change the behavior of the system dramatically, so this needs to be investigated. An algorithm that can reproduce the dynamic spectra of an exomoon from an initial orbital state needs to be build, and followed by the reverse algorithm that can reproduce the orbital state of the exomoon from its dynamic spectra.

There is a new idea on how to use radio emissions to detect exomoons, and it needs to be developed. This idea revolves around the concept of reflection and change of polarization of the circularly polarized signals from an electromotive moon. Whenever light is reflected from a material, the event can change the polarization of the incident light in such a way that it leaves information about the reflective surface. Thus, an exomoon's signal can be reflected off another exomoon, and be redirected towards Earth, now having elliptical polarization rather than circular. Furthermore, there could also be *occultations*, which is an eclipsing event that involves an exomoon blocking the radio emissions due to another exomoon, temporarily keeping them from reaching Earth. In the latter case, if the first exomoon is known to be there, then the occultation will reveal the presence of the second object, which would most likely be an exomoon. These ideas are shown schematically on Figure 7.1.

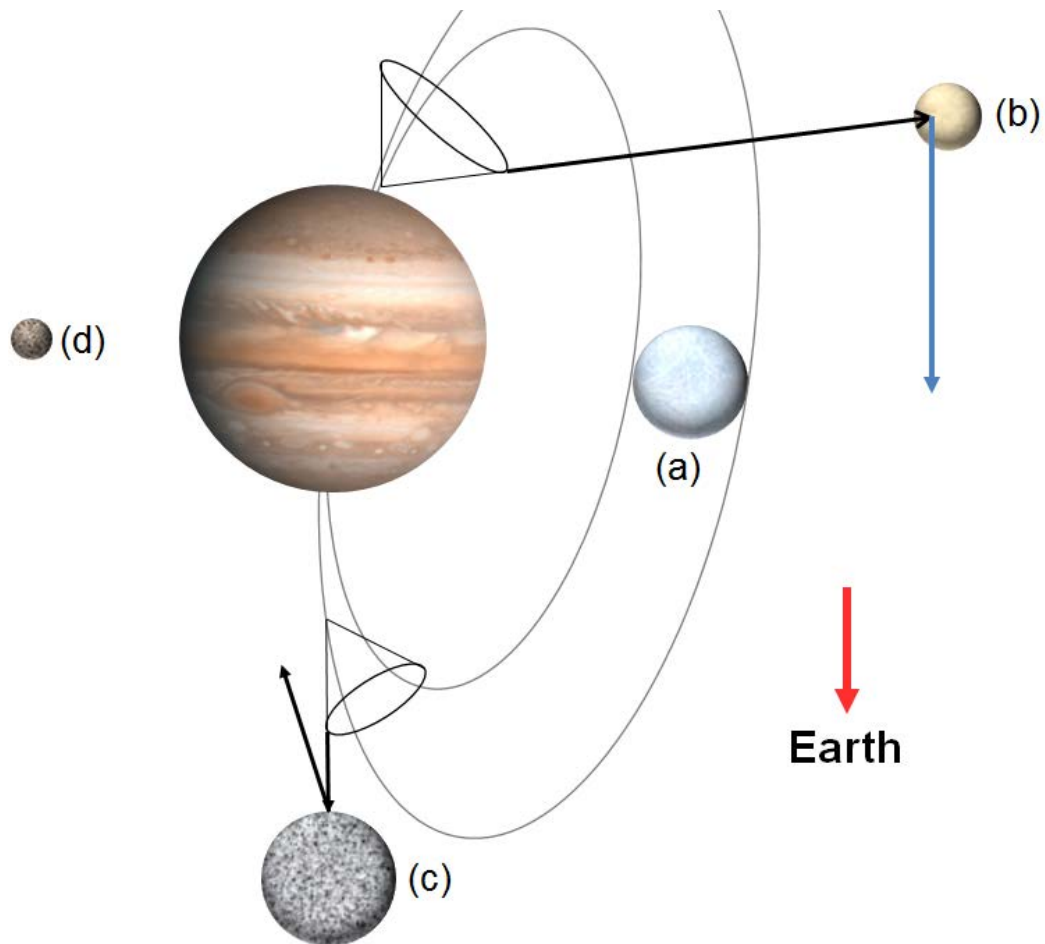


Figure 7.1. Interactions between radio emissions powered by an electromotive moon (a) with secondary moons. Exomoon (c) is occulting the radio signal, while exomoon (b) is reflecting and polarizing the signal, and exomoon (d) is a non-interacting moon.

Finally, if the conductive medium of an electromotive moon is an icy surface rather than an ionosphere, then the joule dissipation from the induction will go directly to heating the ice. If the electromagnetic interaction is strong enough it could melt some of the icy surface, potentially creating a habitable region on the electromotive moon.

Chapter 8

Concluding Remarks

The proposition to detect exomoons from radio signals has given us a brand new opportunity for discovery, while opening the door to a whole new class of instruments to aid us in the search for exomoons. One of these instruments is the Giant Metre Radio Telescope (GMRT) in India, which observed several potential exomoon candidates. The obtained data is being analyzed and the results will be published in the *Astrophysical Journal*. To continue these searches, more time on the GMRT will be requested as well as observational time on the Arecibo Observatory in Puerto Rico and LOFAR in Europe.

In this dissertation I have shown the mechanics of exomoon radio detection, its benefits, and its feasibility for radio astronomical observations. Of particular interest is the case of multiple-moon detections because they provide the most amount of information about the system directly from the observables. Furthermore, my ongoing studies have hinted that exomoon radio signals could even be used to map the surface of an exomoon through the polarization of radio waves reflected off the surface.

I will continue to innovate in this a new area of planetary science, and push the limits of radio telescopes so that perhaps one day soon we will find that little piece of the story that we have long been missing: the exomoons.

Appendix A
Successful Observational Proposal

SEARCH FOR EXTRA-SOLAR MOONS IN 9 NEARBY STAR SYSTEMS

Preamble

The proposal shown below was submitted to GMRT on January 15th, 2015, to request observing time for their 28th observing cycle. Of the originally proposed 9 targets, we were allowed to observe 3, which is a great success given the high risk nature of the proposal.

Abstract

The field of exoplanet detection has seen great innovations since the discovery of the first exoplanet. Observational surveys have led to the confirmation of over 1800 exoplanets in over 400 planetary systems. Given what we know about the solar system, one might expect exomoons to be at least as common. Nonetheless, finding the first exomoon has proved elusive in spite of several projects aim at precisely that purpose. Here we propose to try a new way of searching for these exomoons on 9 nearby star systems, which could lead to that first exomoon confirmation. This new technique is based on a radio wave emitting mechanism seen in our solar system. On Jupiter, the moon Io's motion produces currents along the field lines that connect it to Jupiter's polar regions. The currents generate and modulate radio emissions along their paths via the electron-cyclotron maser instability. In a recent publication, we proposed that this exomoon-planet interaction should exist in other planetary systems, and showed that the resulting radio emissions could be used to discover such exomoons. We chose 11 stars in 9 star systems as observational candidates to perform this search. The targets were selected following various criteria aimed at enhancing our chances of success.

Scientific Justification

INTRODUCTION

Since the discovery of the first confirmed extra solar planet (exoplanet) around the pulsar PSR1257 + 12 (Wolszczan & Frail, 1992), the field of exoplanet detection has been through a great deal of development in techniques and instrumentation. Various

ground-based and space based surveys including Kepler, CoRoT and Keck, have led to the confirmation of over 1800 exoplanets, and thousands of exoplanet candidates identified by the NASA's *Kepler* space telescope. Nonetheless, even with such successful exoplanet finding missions and programs, it has not yet been possible to confirm the existence of a single exomoon.

Based on our knowledge of the solar system, one might expect exomoons to be fairly common, and several potential candidates have already been suggested. On April 2014, a team of scientists led by D. P. Bennett from the University of Notre Dame announced that they had found either a free floating Jovian exoplanet with an Earth-size exomoon, or an exoplanet orbiting a star (Bennett *et al.* 2014). Also on April 2014, L. Ben-Jaffel (University of Paris) and G. E. Ballester (University of Arizona) proposed the existence of two exomoons with plasma tori to explain early ingress absorptions observed on WASP-12b, and HD189733b (Ben-Jaffel *et al.* 2014). Unfortunately, as the study explains, the model used is a work in progress and alternative explanations, though less favoured, do exist. Moreover, Kipping *et al.* (2009) suggested that exomoons may actually be discovered in the data already collected by the *Kepler* mission, though to date no such discovery has been announced. Hence, confirming the discovery of an exomoon continues to prove elusive.

Furthermore, with several Earth-like exoplanets, such as Gliese 832c and Kepler 62e, already discovered, **finding the first confirmed exomoon has arguably become the new Holy Grail of exoplanetary research. The main goal of the proposed observation is to detect the first exomoon by using a new radio detection technique originally suggested by Noyola, Satyal & Musielak (2014, *ApJ*, 791:25, 5pp), and described in this proposal.**

THEORETICAL BACKGROUND

Io is an intensely volcanic moon orbiting inside Jupiter's magnetosphere. The volcanic activity creates a light atmosphere of SO_2 around Io, which ionizes to create an ionosphere (Lopes & Spencer 2007). This ionosphere then injects ions into Jupiter's magnetosphere to create a plasma torus, which orbits Jupiter's magnetic equator at an angle of 9.6° from the rotational equator and co-rotates with the magnetic field at a speed of 74 km s^{-1} (Su 2009). Io orbits Jupiter at a linear speed of 17 km s^{-1} , so Jupiter's magnetic field passes Io at a speed of 57 km s^{-1} . The speed difference gives rise to a *unipolar inductor* (Griessmeier et al. 2007), which induces a current across Io's atmosphere of a few million amps. The current then accelerates the electrons that produce decametric radio emissions, also known as Io-DAM (Crary 1997). It must be noted that while volcanism is essential to the formation of a dense ionosphere around Io, such a process might not be required for larger moons, since moons like Titan are already large enough to sustain a thick atmosphere, which in turn can create an ionosphere.

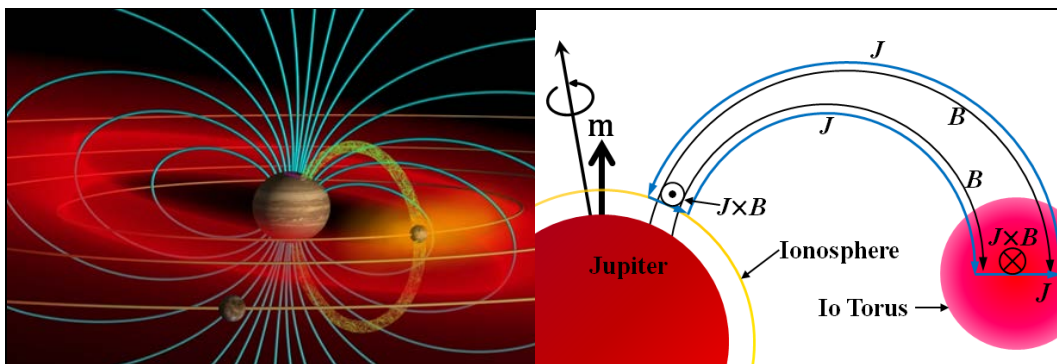


Figure 1. The *left panel* shows the interaction between Jupiter and Io. The cyan coloured lines are Jupiter's magnetic field lines, Io is the moon inside the yellowish glow, the red torus around Jupiter is the plasma torus produced by Io, and the yellow-green arc connecting Jupiter and Io (called the Io flux tube) is where the radio emissions are produced. The *right panel* shows the closed circuit form between Io (not shown) and Jupiter. The unipolar inductor mechanism produces a voltage drop across Io, which generates a current. At the other end of the circuit, the circuit is completed by Jupiter's ionosphere. [Image credit: John Spencer (left) & Joaquin Noyola (right)]

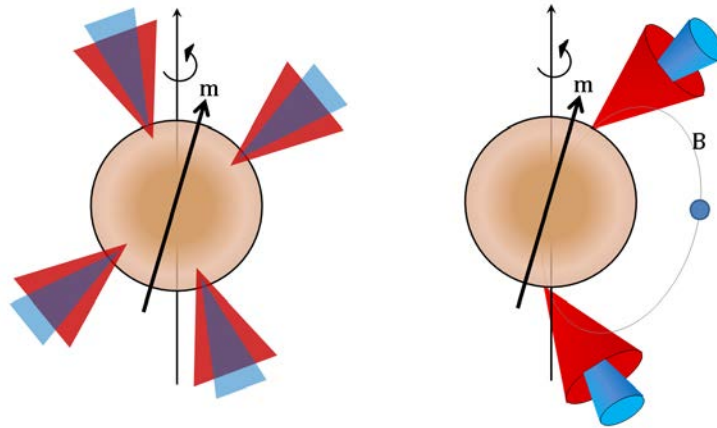


Figure 2. Exoplanet radio emission profiles shown with two arbitrary frequencies (shown as red and blue). The left panel shows the cross-section of the emission geometry for auroral radio emissions not related to the presence of an exomoon. The full emission profile is obtained by rotating the figure around the magnetic moment axis, m . The right panel shows the cones for flux tube radio emissions directly induced by the presence of an exomoon (shown as a blue circle). The axes of the cones are parallel the magnetic field lines at the point of emission. The emission geometries of the two cases are very different, and so produce very different signatures. [Image credit: Suman Satyal & Joaquin Noyola].

Moreover, the interaction between Io and the plasma torus produces Alfvén waves (Belcher 1987). Several analytical and numerical models have been proposed to explain the mechanism by which Alfvén waves interact with the torus. In these models, Alfvén waves generate electric fields parallel to Jupiter’s magnetic field lines, which then transport and accelerate electrons toward Jupiter’s magnetic poles (Su 2009; Saur et al. 1999; Crary 1997; Neubauer 1980 and references therein). The electrons traveling through the field lines create an electron cyclotron maser, which then emits the characteristic radio waves (Crary 1997; Mauk et al. 2001). This planet-moon interaction forms the closed circuit shown on Figure 1. The other Galilean moons, as well as Titan and Enceladus on Saturn, also show this effect, although the emitted power is noticeably smaller. In other words, these radio wave emitting moon-planet interactions are common in our solar system, so it is natural to expect them to exist in other solar systems as well.

In our recent publication (Noyola, et al., 2014), we proposed that the interaction between Io and the Jovian magnetosphere could also be found in exoplanet-moon pairs,

and the resulting radio emissions could be used to directly detect these systems. As an example, we used our theory to predict that an exomoon as small as Europa (0.24 Earth radii) could be detected around Eps Eridani b, a 1.55 Jupiter mass exoplanet 10.5 light-years from Earth, by a radio telescope with capability of $50 \mu\text{Jy}$ sensitivity, assuming that the exomoon provides an amount of plasma similar to that provided by Io. Additionally, we highlighted several advantages that this detection method has over others, including that it favours exomoons orbiting *cold Jovians*, and that it works even if the system's orbital plane is not aligned with our line of sight. Finally, radio detection constitutes a *direct confirmation* of both, the exomoon and its Jovian host, because the emission geometry of these systems (and thus their signature in the frequency-time plane) is very unique. To illustrate, Figure 3 compares the emission geometries of an exoplanet's auroral radio emissions, which are not related to the presence of an exomoon, and exomoon-induced radio emissions.

The main result arising from our publication was the more general prediction of what types of exomoons would be observable (see Figure 3). We obtained the plots shown in Figure 3 by first assuming Jupiter-like gas giants in terms of planetary radius and rotation rate, and a distance from Earth of 15 light years. Then we calculated the minimum radius of an exomoon that is needed for the exomoon to be detectable from

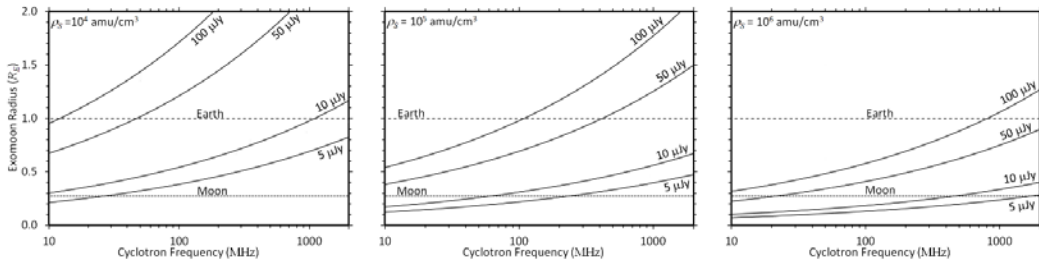


Figure 3. The minimum required radii of detectable exomoons that are 15 light years away are plotted as a function of the system's emission frequency (the cyclotron frequency) for several flux sensitivity values. From left to right, the panels show results for plasma densities of 10^4 , 10^5 , and 10^6 amu cm^{-3} . $1 \text{ Jy} = 10^{-26} \text{ Wm}^{-2} \text{ Hz}^{-1}$ (Noyola, et al., 2014).

Earth by telescopes of various sensitivities.

There are several previous studies that are at least partially based on the Jupiter–Io system, and in which the authors suggest detecting exoplanets by using exoplanetary radio emissions (Lazio et al. 2004 and references therein). However, those authors based their studies on the non-Io-controlled decametric Jovian emissions, which are induced by the stellar wind rather than Io. This exoplanet radio detection favours hot Jupiters, just as detection by transit and radial velocity methods do. Moreover, Dr. Jonathan Nichols studied Jupiter’s magnetosphere–ionosphere coupling mechanism and hypothesized that this mechanism could produce enough radio power to be detectable from Earth (Nichols 2011). Both his study and ours are based on the unipolar inductor mechanism and the current source is Io’s plasma torus. However, the circuit made by the current in each case is fundamentally different. In our study, the circuit directly couples Io to Jupiter’s poles, whereas in Nichols’s study, the current bypasses Io and instead flows through magnetic field lines well beyond the moon. As with the other studies mentioned above, Nichols’s mechanism favours exoplanets in small orbits. Specifically, it requires large X-ray and EUV stellar irradiation of the exoplanet’s ionosphere to produce a large enough output power to make it detectable.

Our detection method does not have such a requirement. In fact, our technique favours exomoons with exoplanets in large orbits because otherwise the stellar wind and irradiation would produce a significant amount of interference (see the left panel on Figure 4). More importantly, even though Nichols emphasizes active moons as the sources of plasma, this might not be the case. Recent computational studies have shown that stellar irradiation alone can ionize the hydrogen-rich atmosphere of a Jovian exoplanet to levels that can match and even vastly exceed the amount of plasma in Io’s

plasma torus (Trammell *et al.* 2014). In other words, Nichols’s mechanism cannot be used to detect exomoons, only exoplanets.

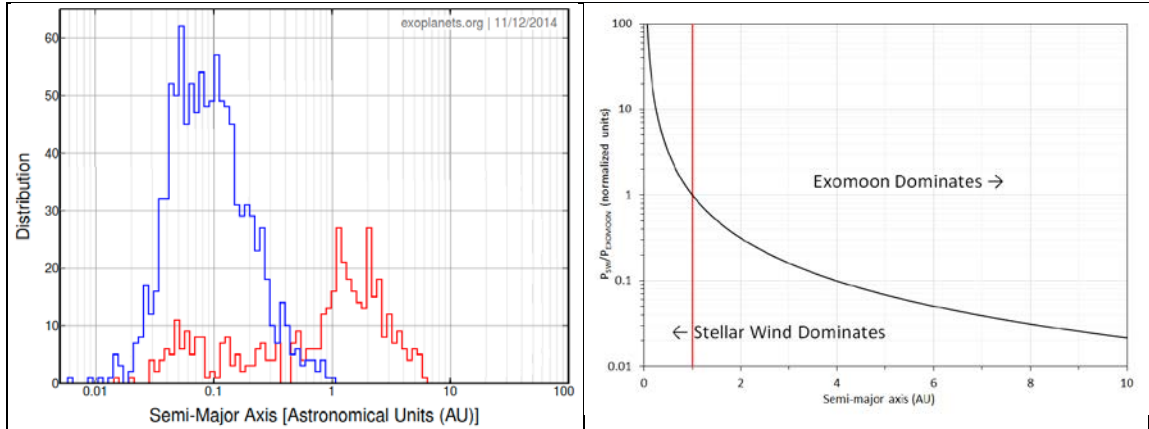


Figure 4. The *left panel* shows a histogram of confirmed exoplanets discovered through transit (blue) and radial velocity (red) techniques. Both of these detection techniques are biased toward smaller orbits. The *right panel* shows how the interference from the stellar wind decays with increasing semi-major axis. The plot’s vertical units are adjusted so that the radio power induced by the stellar wind, P_{SW} , and the radio power induced by an exomoon, $P_{EXOMOON}$, are equal at 1 AU from the star (red line). [Image credit: *Exoplanets.org* (left) & *Joaquin Noyola* (right)].

SELECTED TARGETS AND EXPECTATIONS

Our targets were selected through a process of elimination involving various theoretical and observational criteria, as explained in the following paragraphs. Nonetheless, *we also welcome target suggestions from the programme committee.* The complete list of targets is shown in

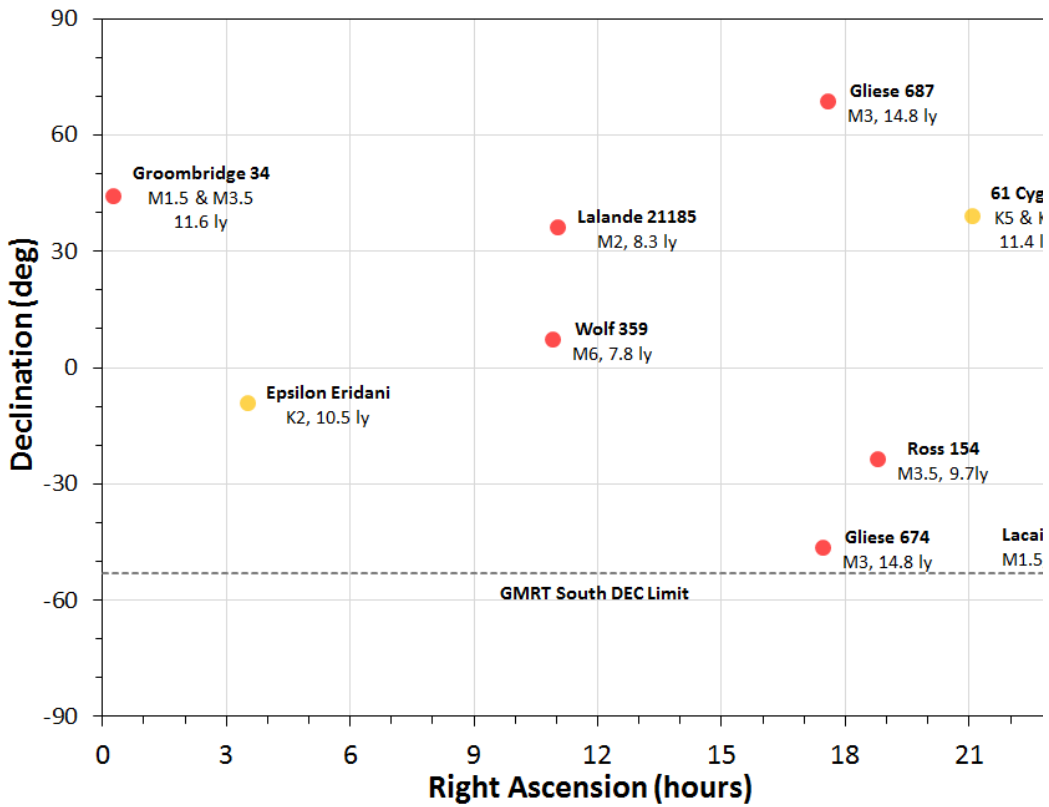


Figure 5. Complete list of targets plotted according to their location. Spectral type and distance from Earth for each star system is also given. [Image credit: Joaquin Noyola]

The first target requirement is that its declination must be between -54° and $+90^{\circ}$, so that it can be observed with GMRT. Secondly, the star must be relatively close to Earth to give us a higher chance of success. Specifically, all of our targets are closer than 15 light years.

Additionally, we wanted stars with either confirmed exoplanets, or likely to have exoplanets. There are only a few exoplanets within 15 light years from Earth (e.g. Epsilon Eridani), so we decided to use star metallicity as a restriction instead, since it is usually believed that stars with higher metallicity have a higher chance of forming planetary systems. All the targets in our selection have a metallicity similar to the sun's ($[Fe/H] \geq -$

0.3). Next we constrained stars based on mass. Formation models predict that even small stars can form gas giants. For example,

Figure 6 displays the expected mass distribution of planets around an M type star of 0.5 solar masses (Alibert *et al.* (2011)). Clearly, even very massive Jovian exoplanets could be expected to form around small stars. However, planet formation does decrease with decreasing star mass, so we limited our search to M dwarfs and larger stars. We also excluded white dwarfs due to the uncertainties in estimating the original star's metallicity and mass.

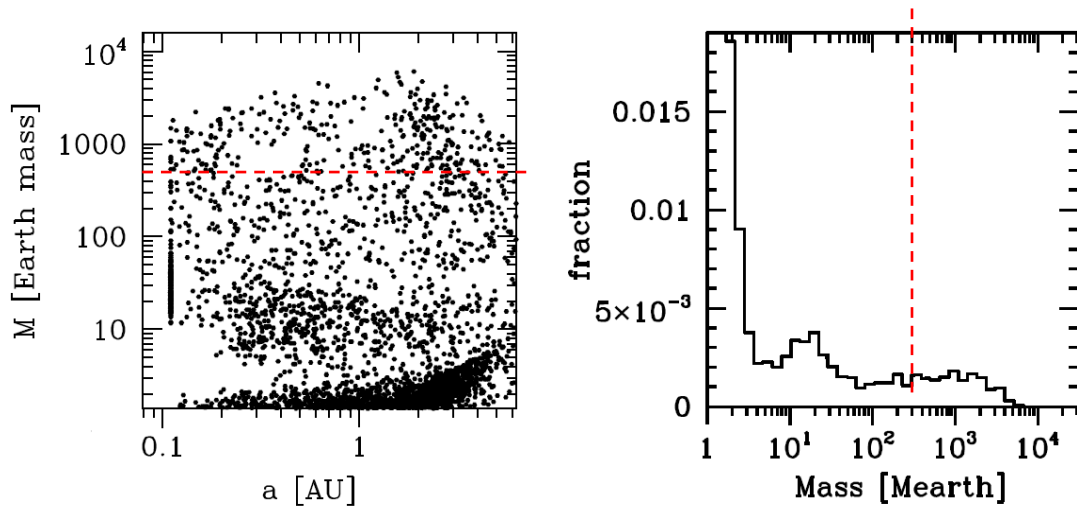


Figure 6. Expected mass distribution of planets around a star of 0.5 solar masses. The left panel shows the distribution of masses vs semi-major axis found through computational formation models. The right panel shows the mass function of all resulting planets as a fraction of the primary mass. In both panels, the red dotted line represents 1 Jupiter mass. Plots adapted from Alibert *et al.* (2011).

Furthermore, in the frequencies available to GMRT we expect to find Jovian planets with masses larger than Jupiter. Formation models show that moons can form around Jovian planets with masses up to 10^{-4} times the mass of their host planet (Canup *et al.* 2006). Thereby, it is not unreasonable to expect Mars-size exomoons orbiting the aforementioned exoplanets. Therefore, we are very confident that at least a few of these

stars will have large cold Jovians, and that these Jovian exoplanets will have plenty of exomoons orbiting them. We are also reasonably confident that at least one of these exomoons could be found with this search.

However, even the case where no exomoon is detected can tell us a lot about the system being observed. The power output of the radio emissions is related to the system's physical properties in such a way that a null result can allow us to place limits on the types of exomoons and exoplanets that may orbit a star. This is especially true in the case of Epsilon Eridani b, where the mass, radius, and orbital parameters of the exoplanet are well known, allowing us to constrain the size and ionospheric density of the exomoon, as well as the magnetic dipole moment of the exoplanet. This limits, combined with results from planet formation simulations can potentially give us a good idea of the kinds of bodies that may be found in a given system. In other words, our technique can serve as a way to detect exomoons or eliminate exomoon candidates.

CONCLUSION

We propose to search for exomoons by using our recently published theory as well as some observational constraints to select the best exomoon candidates. We believe the search outlined in this proposal has a good chance of detecting first exomoon!

Appendix B

Simulation Program to Calculate Exomoon Radio Power

```

1 package moonpower;
2 import java.awt.*;
3 import java.io.*;
4 import javax.swing.*;
5 import java.text.*;
6
7 /**
8  * @(#)MoonData.java
9  *
10 * MoonData application
11 *
12 * Joaquin P Noyola
13 * @version 1.00 2013/6/19
14 * @last modified 2013/12/29
15 */
16 public class MoonData
17 {
18     /**Conversion factors*/
19     public static final double Jy = 1e-26;//1 Jansky = 1e-26 W/m^2•Hz
20     public static final double AU = 1.495978707e11;//meters
21     public static final double pc = 3.08567758e16;//meters
22     public static final double ly = 9.4605284e15;//meters
23     public static final double Msun=1.989e30;//kg Mass of the sun
24     public static final double RE = 6.371e6;//meters, Earth radius
25     public static final double amu=1.66053892e-27;//kg, atomic mass units
26     /**Constants*/
27     public static final double G = 6.67398e-11;// Gravitational constant
28     public static final double mu0 = 4*Math.PI*1e-7;//A•m^2, Permeability of free space
29     public static final double NA = 6.0221415e23;//atoms/mol, Avogadro's number
30     public static final double sigmaH = 2.0e5;//S/m, liquid metallic hydrogen conductivity
31     /**Jupiter Data*/
32     public static final double MJ = 1.89813e27;//kg
33     public static final double RJ = 6.9911e7;//meters
34     public static final double rJ = 7.785e11;//meters
35     public static final double TJ = 35760;//seconds
36     public static final double wJ = 2*Math.PI/TJ;//rad/s
37     public static final double SGJ = 1.326;//Specific gravity. NOTE: Saturn's is 0.7
38     /**Io Data*/
39     public static final double MIo = 8.9319e22;//kg
40     public static final double RIo = 1.8213e6;//meters
41     public static final double rIo = 4.217e8;//meters
42     //For Io, rhoN = 7e-17 kg/m^3, and for Earth rhoN = 2.7e-15 kg/m^3
43     public static final double rhoN = 1.66053892e-15;//kg/m^3, plasma density
44     public static final double beta = 0.01;//Radio emission efficiency
45
46     public static void main(String[] args)
47     {
48         //simulation parameters
49         int mode = 0;//Use 0 for prad, 1 for pC, and 2 for pminus
50         double retro = 1.0;//Use -1 for prograde, and +1 for retrograde moons

```

```

51 //double SG = SGJ;//planet's specific gravity
52 double minMP = 0.1*MJ;//Starting planet mass, usually =MJ
53 double MaxMP = 15.0*MJ;
54 double dM = MJ/100.0;//mass increase per iteration
55 double wP = wJ;//planet's angular velocity
56 //double rhoS = 5500;//kg/m^3, assumed moon density
57 double K = 1.15;//exponent on magnetic moment law, was 1.148
58 double Omega = 0.2;//steradians
59 //double f=0.257; double k2P = 0.51; double QP = 1.0e5;
60 //double life = 1.0;//age of the moon as a fraction of the star's age
61 //double rP = rJ;//planet's semi-major axis
62 double minS = 1e-30;//min estimated flux (0.1 mJy)
63 double MaxS = 1e-28;//maximum estimated flux (10 mJy)
64 //simulation variables
65 //double MaxMS;//Maximum satellite mass for a given MP
66 double RS;//Moon radius
67 double RP;//planet's predicted radius from mass and SG
68 double fc;//the cyclotron frequency
69 double rS;
70 double rMin;//starting moon orbital radius for B optimization
71 double rOpt = 0;//optimal orbital radius
72 double rSminus = 0;//<rOpt but 90% Pmax
73 double rSplus = 0;//>rOpt but 90% Pmax
74 double[] rScontour = {0.5, 0.6, 0.7, 0.8, 0.9, 0.95};//array for rOpt vs MP, contour lines
//are rScontour[x]*maxPrad = const
75 double[][] rOptGraph = new double[(int)((MaxMP-minMP)/dM +
1.5)][2*rScontour.length + 2];//data for rOpt vs MP contour map
76 double drS;//increment in rS for optimizing B
77 double maxPrad = 0;//Maximum radio power
78 double m;//magnetic dipole moment in A*m^2 or J/T
79 double BS;//current magnetic field strength at satellite
80 double V0;//plasma's speed relative to Io
81 double rhoC = 0;//critical plasma density for given system
82 double Irad = 0;//Radio power output/RS^2, Intensity per unit moon cross section
83 double Imax = 0;
84 double Inext = 0;//next radio power output/RS^2
85 double[][] data = new double[(int)((MaxMP-minMP)/dM +
1.5)][(int)(Math.log10(MaxS/minS)+1.5 + 6)];
86 int row;
87 //Star Information
88 /**Proxima Centauri*/
89 //double Mstar = 0.123*Msun;
90 double d = 15*ly;//Distance to the host star
91 //double age = 4.85e9*365.25*24*3600;//seconds, age of the star
92 /**/
93
94 /*Obtaining output file, written for GNU Plot (Column format)*/
95 Frame codeDisplay = new Frame();
96 codeDisplay.setLocation(100,100);
97 File output = null;

```

```

98     File rOptFile = null;
99     int returnVal;
100    JFileChooser chooser = new JFileChooser();
101        chooser.setDialogTitle("Choose the location of the output files");
102        chooser.setDialogType(JFileChooser.SAVE_DIALOG);
103        chooser.setFileSelectionMode(JFileChooser.DIRECTORIES_ONLY);
104
105    returnVal = chooser.showSaveDialog(codeDisplay);
106    if(returnVal == JFileChooser.APPROVE_OPTION)
107    {
108        String path = chooser.getSelectedFile().getPath();
109        output = new File(path + "\\flux.csv");
110        rOptFile = new File(path + "\\rOpt.csv");
111        // System.out.println(output.getPath());//Debugging line
112    }
113    else
114    {
115        JOptionPane.showMessageDialog(null,"No output file selected.\nProgram will
terminate.",
116                                     "Exiting",JOptionPane.ERROR_MESSAGE);
117        System.exit(0);
118    }
119
120    //Performing Calculations
121    RP = RJ;//Assuming constant radius
122    for(double MP = minMP; MP < MaxMP; MP += dM)
123    {
124        row = (int)((MP-minMP)/dM+0.5);//!!!!!!!!!!!!!!!!!!!!!!!!!!!!!!
125        data[row][0] = MP/MJ;//First column*****
126        rOptGraph[row][0] = MP/MJ;//First column*****
127        //System.out.println("row="+row+", MP="+MP/MJ);//Debugging line
128        //next two columns
129        //RP = Math.pow(MP*SGJ/(MJ*SG),1.0/3.0)*RJ;//Substitute with formula
130        m = 1e-5*Math.pow(MP*sigmaH*wP/(2*Math.PI),K);//(A*m^2)@Durand-Manterola
(2009)
131        /** Assuming interaction occurs at the pole
132        fc = 2.35e7*(wP/wJ)*Math.pow(MP/MJ,5.0/3)*Math.pow(RJ/RP,3);//(Hz)@Farrel
(2004)
133        /**/
134        data[row][1] = m;
135        data[row][2] = fc/1e6;//(MHz)
136
137        //Finding optimal rS
138        rMin = Math.pow(G*MP/(wP*wP),1.0/3.0);//synchronous orbit
139        drS = rMin/1000;//step in rS
140        double invrs3 = 0;
141        for(rS=rMin; rS<20*rMin; rS += drS)
142        {
143            invrs3 = 1.0/Math.pow(rS,3);
144            V0 = rS*Math.abs(wP + retro*Math.sqrt(G*MP*invrs3));

```

```

145     BS = 1e-7*m*invrs3;
146     /**
147     Irad = MoonData.Irad_calc(mode, BS, V0);
148     /**/
149     if(Irad > Imax)
150     {
151         rOpt = rS;
152         Imax = Irad; //saving maximum radio power found
153         //System.out.println("pmax = " + pmax); //Debugging line
154     }
155 }
156 //Finding rSminus and rSplus
157 Irad = 0;
158 boolean min=true, max=true;
159 for(rS=rMin; rS<20*rMin; rS += drS)
160 {
161     invrs3 = 1.0/Math.pow(rS,3);
162     V0 = rS*Math.abs(wP + retro*Math.sqrt(G*MP*invrs3));
163     BS = 1e-7*m*invrs3;
164     /**
165     Irad = MoonData.Irad_calc(mode, BS, V0);
166     /**/
167     if(min || max)
168     {
169         Inext = Irad/Imax; //pnext is unitless here, it is not power/Area
170         if(rS < rOpt && Inext >= 0.95)
171         {
172             if(min)
173             {
174                 rSminus = rS;
175                 min = false;
176                 //System.out.println("rSminus: prad/pmax = " + pnext); //Debugging line
177             }
178         }
179         else if(rS > rOpt && Inext <= 0.95)
180         {
181             if(max)
182             {
183                 rSplus = rS;
184                 max = false;
185                 //System.out.println("rSplus: prad/pmax = " + pnext); //Debugging line
186             }
187         }
188     }
189     else if(!min && !max) break;
190 }
191 //System.out.println(rSminus/RJ + "\t" + rOpt/RJ + "\t" + rSplus/RJ); //Debugging line
192
193 //Saving rS data
194 rOptGraph[row][6] = rSminus/RJ;

```

```

195     rOptGraph[row][7] = rOpt/RJ;
196     rOptGraph[row][8] = rSplus/RJ;
197     //Finding rhoC at rOpt
198     invrs3 = 1.0/Math.pow(rOpt,3);
199     V0 = rOpt*Math.abs(wP + retro*Math.sqrt(G*MP*invrs3));
200     BS = 1e-7*m*invrs3;
201     rhoC = Math.pow(BS/V0,2)/mu0;
202     //Debugging line
203     //System.out.println("V0="+V0+", BS="+BS+", rhoC="+rhoC);
204     data[row][3] = rhoC*1e-6/amu;//(amu/cm^3)
205     data[row][4] = BS;//(Tesla) BS @ rOpt
206     //System.out.print(row + "\t");//Debugging line
207
208     //Looping through the flux lines, using rhoN = rhoC
209     Imax = MoonData.Irad_calc(mode, BS, V0);
210     data[row][5] = Imax;
211     int col = 6;//column counter
212     for(double S=minS; S<=MaxS; S *= 10)//wrong? need to fix?
213     {
214         //System.out.print(col + "\t");
215         RS = d*Math.sqrt(fc*Omega*S/(2.0*Imax));
216         data[row][col] = RS/RE;//*****
217         col++;
218     }
219     //System.out.println("");
220     //System.out.println("\n" + data[row][0] + "\t" + data[row][1] + "\t" + data[row][2] +
221     "\t" + data[row][3] + "\t" + data[row][4] + "\t" + data[row][5]);
222 }
223 try
224 {
225     //File Writers
226     FileWriter fstream1 = new FileWriter(output);
227     BufferedWriter out1 = new BufferedWriter(fstream1);
228     out1.write("#MP(MJ),m(Am^2),fc(MHz),rhoC(amu/cm^3),BS@rOpt(T),"
229     +"Imax(W/m^2),RS@0.1mJy(RE),RS@1mJy(RE),RS@10mJy(RE)\n");//header1
230     FileWriter fstream2 = new FileWriter(rOptFile);
231     BufferedWriter out2 = new BufferedWriter(fstream2);
232     //Building the overly complicated header for rOpt.csv
233     String header2 = "#MP(MJ),";
234     for(int i=0; i<rScontour.length; i++)
235     {
236         header2 += "rS@"+rScontour[i]+"(RJ),";
237     }
238     header2 += "rOpt(RJ),";
239     for(int i=rScontour.length-1; i>=0; i--)
240     {
241         header2 += "rS@"+rScontour[i]+"(RJ),";
242     }
243     header2 += "\n";

```

```

244     out2.write(header2);
245     DecimalFormat F = new DecimalFormat("#.#####");
246     //Writing to flux.csv and rOpt files
247     for(int j=0; j<data.length; j++)
248     {
249         for(int k=0; k<data[j].length; k++)
250         {
251             out1.write(F.format(data[j][k]) + ",");
252         }
253         out1.write("\n");
254         for(int k=0; k<rOptGraph[j].length; k++)
255         {
256             out2.write(F.format(rOptGraph[j][k]) + ",");
257         }
258         out2.write("\n");
259     }
260
261     out1.close();//Save file and close it
262     out2.close();//Save file and close it
263 }
264 catch (Exception e)//Catch exception if any
265 {
266     JOptionPane.showMessageDialog(codeDisplay, "Error: " + e.getMessage(),
267         "Error", JOptionPane.ERROR_MESSAGE);
268     System.exit(0);
269 }
270 /**/
271 System.exit(0);
272
273 }
274
275 /**Different ways of calculating Prad
276 * mode 1 corresponds to pC
277 * mode 2 corresponds to pminus
278 * all other modes correspond to the full prad calculation
279 * NOTE: pplus is just sqrt(2)*pC, so use mode 1
280 */
281 public static double Irad_calc(int mode, double bs, double v0)
282 {
283     if (mode == 1)
284         return Math.PI*beta*bs*bs*v0/(Math.sqrt(2.0)*mu0);
285     else if (mode == 2)
286         return Math.PI*beta*bs*v0*v0*Math.sqrt(rhoN/mu0);
287     else
288         return 2.5e6*beta*Math.pow(v0*bs,2)/Math.sqrt(bs*bs/(mu0*rhoN)+v0*v0);
289 }
290 }

```

References

- Acuña, M. H., Neubauer, F. H. & Ness, N. F., 1981. Standing Alfvén wave current system at Io - Voyager 1 observations. *Journal of Geophysical Research*, Volume 86, pp. 8513-8521.
- Agnor, C. B. & Hamilton, D. P., 2006. Neptune's capture of its moon Triton in a binary-planet gravitational encounter. *Nature*, 441(7090), pp. 192-194.
- Alibert, Y., Mordasini, C. & Benz, W., 2011. Extrasolar planet population synthesis. III. Formation of planets around stars of different masses. *Astronomy and Astrophysics*, Volume 526, pp. A63, 12 pp..
- Bagenal, F., 1994. Empirical model of the Io plasma torus: Voyager measurements. *Journal of Geophysical Research*, 99(A6), pp. 11043-11062.
- Bagenal, F. & Delamere, P. A., 2011. Flow of mass and energy in the magnetospheres of Jupiter and Saturn. *Journal of Geophysical Research*, 116(A5), p. A05209.
- Belcher, J., 1987. The Jupiter-Io connection - an Alfvén engine in space. *Science*, Volume 238, pp. 170-176.
- Ben-Jaffel, L. & Ballester, G. E., 2014. Transit of Exomoon Plasma Tori: New Diagnosis. *The Astrophysical Journal Letters*, 785(2), pp. L30-L35.
- Bigg, E. K., 1964. Influence of the Satellite Io on Jupiter's Decametric Emission. *Nature*, Volume 203, pp. 1008-1010.
- Campante, T. L. et al., 2015. An Ancient Extrasolar System with Five Sub-Earth-size Planets. *ApJ*, 799(2), p. 170.
- Canup, R. M. & Ward, W. R., 2006. A common mass scaling for satellite systems of gaseous planets. *Nature*, 441(7095), pp. 834-839.
- Crary, F. J., 1997. On the generation of an electron beam by Io. *JGR*, Volume 102, pp. 37-50.

- Cuntz, M., Quarles, B., Eberle, J. & Shukayr, A., 2013. On the Possibility of Habitable Moons in the System of HD 23079: Results from Orbital Stability Studies. *PASA*, Volume 30, p. 33.
- Cuntz, M. & Yeager, K. E., 2009. On the Validity of the "Hill Radius Criterion" for the Ejection of Planets from Stellar Habitable Zones. *The Astrophysical Journal Letters*, 697(2), pp. L86-L90.
- Durand-Manterola, H. J., 2009. Dipolar magnetic moment of the bodies of the solar system and the Hot Jupiters. *P&SS*, 57(12), p. 1405.
- Galilei, G., 1989. *Sidereus Nuncius*. Chicago & London: University of Chicago Press.
- Goldreich, P. & Lynden-Bell, D., 1969. Io, a jovian unipolar inductor. *Astrophysical Journal*, Volume 156, pp. 59-78.
- Griessmeier, J. M., Zarka, P. & Spreeuw, H., 2007. Predicting low-frequency radio fluxes of known extrasolar planets. *A&A*, Volume 475, pp. 359-368.
- Heller, R. & Pudritz, R., 2015. Water Ice Lines and the Formation of Giant Moons around Super-Jovian Planets. *The Astrophysical Journal*, 806(2), pp. 181-189.
- Hess, S., Cecconi, B. & Zarka, P., 2008. Modeling of Io-Jupiter decameter arcs, emission beaming and energy source. *Geophysical Research Letters*, 35(13), p. L13107.
- Hess, S. L. G. & Zarka, P., 2011. Modeling the radio signature of the orbital parameters, rotation, and magnetic field of exoplanets. *Astronomy & Astrophysics*, Volume 531, p. A29.
- Hughes, D. W., 2003. Planetary spin. *Planetary and Space Science*, 51(7-8), pp. 517-523.
- Jackson, J. D., 1999. *Classical Electrodynamics*. 3rd ed. United States of America: Wiley.

- Johnson, R. E. & Huggins, P. J., 2006. Toroidal Atmospheres around Extrasolar Planets. *The Publications of the Astronomical Society of the Pacific*, 118(846), pp. 1136-1143.
- Joseph, T. et al., 2004. The Radiometric Bode's Law and Extrasolar Planets. *ApJ*, Volume 612, pp. 511-518.
- Kallenrode, M.-B., 2004. *Space Physics*. 3rd ed. Berlin: Springer.
- Kassim, N. E. et al., 2005. *The Long Wavelength Array*. Santa Fe, New Mexico, s.n.
- Kipping, D. M. et al., 2013. The Hunt for Exomoons with Kepler (HEK). I. Description of a New Observational project. *ApJ*, 750(2), p. 115.
- Kivelson, M. G., 2004. *Jupiter*. Cambridge: Cambridge University Press.
- Koskinen, T. T., Yelle, R. V., Lavvas, P. & Lewis, N. K., 2010. Characterizing the Thermosphere of HD209458b with UV Transit Observations. *The Astrophysical Journal*, 723(1), pp. 116-128.
- Lazio, W. T. J. et al., 2004. The Radiometric Bode's Law and Extrasolar Planets. *ApJ*, 612(1), pp. 511-518.
- Lopes, R. M. & Spencer, J. R., 2007. Io After Galileo: A New View of Jupiter's Volcanic Moon. Berlin: Springer.
- Marois, C. et al., 2010. Images of a fourth planet orbiting HR 8799. *Nature*, 468(7327), pp. 1080-1083.
- Mauk, B. H., Williams, D. J. & Eviatar, A., 2001. Understanding Io's space environment interaction: Recent energetic electron measurements from Galileo. *JGR*, Volume 106, pp. 26195-26208.
- Mayor, M. & Queloz, D., 1995. A Jupiter-mass companion to a solar-type star. *Nature*, 378(6555), p. 355-359.

- Mordasini, C. et al., 2012. Characterization of exoplanets from their formation. II. The planetary mass-radius relationship. *Astronomy & Astrophysics*, Volume 547, pp. A112-A147.
- Musielak, D. E. & Musielak, Z. E., 2011. *Detection of Moons around Giant Exoplanets*. Seattle, WA, American Astronomical Society.
- Musielak, Z. E. & Quarles, B., 2014. The three-body problem. *Reports on Progress in Physics*, 77(6), p. 065901.
- Neubauer, F. M., 1980. Nonlinear standing Alfvén wave current system at Io - Theory. *JGR*, Volume 85, pp. 1171-1178.
- Nichols, J. D., 2011. Magnetosphere-ionosphere coupling at Jupiter-like exoplanets with internal plasma sources: implications for detectability of auroral radio emissions. *MNRAS*, 414(3), pp. 2125-2138.
- Noyola, J. P., Satyal, S. & Musielak, Z. E., 2014. Detection of Exomoons Through Observation of Radio Emissions. *ApJ*, Volume 791, p. 25.
- Noyola, J. P., Satyal, S. & Musielak, Z. E., 2015. On the radio detection of multiple-exomoon systems due to plasma torus sharing. *Under review by the Astrophysical Journal*.
- Pierson, H. O., 1993. Handbook of carbon, graphite, diamond, and fullerenes: properties, processing, and applications. Park Ridge, N.J., U.S.A: Noyes Publications.
- Porter, S. B. & Grundy, W. M., 2011. Post-capture Evolution of Potentially Habitable Exomoons. *Astrophysical Journal*, 736(1), p. L14.
- Quarles, B., Musielak, Z. E. & Cuntz, M., 2012. Habitability of Earth-mass Planets and Moons in the Kepler-16 System. *ApJ*, 750(1), p. 14.
- Queinnee, J. & Zarka, P., 2001. Flux, power, energy and polarization of Jovian S-bursts. *Planetary and Space Science*, 49(3-4), pp. 365-376.

- Santos, N. C., Israelian, G. & Mayor, M., 2004. Spectroscopic [Fe/H] for 98 extra-solar planet-host stars. Exploring the probability of planet formation. *Astronomy and Astrophysics*, Volume 415, pp. 1153-1166.
- Saur, J., Neubauer, F. M., Strobel, D. F. & Summers, M. E., 1999. Three-dimensional plasma simulation of Io's interaction with the Io plasma torus: Asymmetric plasma flow. *Journal of Geophysical Research*, 104(A11), pp. 25105-25126.
- Schunk, R. & Nagy, A., 2009. *Ionospheres: Physics, Plasma Physics, and Chemistry*. 2nd ed. Cambridge: Cambridge University Press.
- Seager, S., 2010. *Exoplanets*. 1st ed. Tucson, AZ: University of Arizona Press.
- Shvets, V. T., 2007. Electrical conductivity of metallic hydrogen in the nearly-free-electron model. *The Physics of Metals and Metallography*, 103(4), pp. 330-336.
- Siscoe, G. L. et al., 1981. Ring current impoundment of the Io plasma torus. *Journal of Geophysical Research*, Volume 86, pp. 8480-8484.
- Snellen, I. A. G. et al., 2014. Fast spin of the young extrasolar planet β Pictoris b. *Nature*, 509(7498), pp. 63-65.
- Su, Y.-J., 2009. *Electromagnetic interaction between Jupiter's ionosphere and the Io plasma torus*. s.l., Proceedings of the International Astronomical Union, pp. 271-282.
- van Haarlem, M. P. et al., 2013. LOFAR: The LOw-Frequency ARray. *Astronomy & Astrophysics*, Volume 556, pp. A2, 53 pp..
- Vidotto, A. A., Jardine, M. & Helling, C., 2011. Prospects for detection of exoplanet magnetic fields through bow-shock observations during transits. *MNRAS*, 411(1), pp. L46-L50.

- Winterhalter, D. et al., 2015. Analysis Update of LOFAR Data from HD 80606b Near Planetary Periastron. In: *EGU General Assembly Conference Abstracts, Vol. 17*. Vienna, Austria: EGU General Assembly Conference Abstracts, p. 14693.
- Wolszczan, A. & Frail, D. A., 1992. A planetary system around the millisecond pulsar PSR1257 + 12. *Nature*, Volume 355, pp. 145-147.
- Zarka, P., 1998. Auroral radio emissions at the outer planets: Observations and theories. *JGR*, Volume 103, pp. 20159-20194.
- Zarka, P., 2007. Plasma interactions of exoplanets with their parent star and associated radio emissions. *Planetary and Space Science*, 55(5), pp. 598-617.
- Zarka, P., Treumann, R. A., Ryabov, B. P. & Ryabov, V. B., 2001. Magnetically-Driven Planetary Radio Emissions and Application to Extrasolar Planets. *Ap&SS*, Volume 277, pp. 293-300.

Biographical Information

Joaquin Noyola first attended UTA in 2004 as an undergraduate student. As an undergraduate student, Joaquin studied fast proton detectors under Dr. Andrew Brandt, and Positron annihilation spectroscopy under Dr. Alex Weiss. He received his B.S. in Physics from UTA in 2009. That same year Joaquin began his graduate studies at UTA, where he studied electrodeposition of photovoltaic materials under Dr. Qiming Zhang, and received his M.S. in Physics in 2013.

After obtaining his M.S. degree, Joaquin began his Ph.D. studies in Astrophysics under Dr. Zdzislaw Musielak where, under his advisor's suggestion, he developed the model for exomoon detection using radio telescopes instead of optical telescopes.